A STUDY OF PROTOPLANETARY DISK EVOLUTION

IN INFRARED CO EMISSION

by

Michael Allan Sánchez, B.S.

A thesis submitted to the Graduate Council of
Texas State University in partial fulfillment
of the requirements for the degree of
Master of Science
with a Major in Physics
August 2021

Committee Members:

Andrea Banzatti, Chair

Blagoy Rangelov

Donald Olson

FAIR USE AND AUTHOR'S PERMISSION STATEMENT

Fair Use

Duplication Permission

DEDICATION

This work is eternally dedicated to my mother, my father, and my sisters.

Este trabajo está eternamente dedicado a mi madre, mi padre, y mis hermanas.

ACKNOWLEDGEMENTS

This work includes observations from the NASA/ESA Hubble Space Telescope. Support for Program GO-14703 was provided through a grant from the Space Telescope Science Institute (STScI) under NASA contract NAS5-26555.This work includes data taken with Cryogenic Infrared Echelle Spectrograph (CRIRES) at the Very Large Telescope (VLT) under program 179.C-0151 (PI K. Pontoppidan), and data taken with iSHELL at the IRTF under program 2016B049 (PI: A. Banzatti). We thank John Rayner for assistance with the iSHELL observations.

TABLE OF CONTENTS

Page

LIST OF TABLES

Table **Page**

LIST OF FIGURES

Figure **Page**

LIST OF ABBREVIATIONS

Abbreviation	Description
AU	Astronomical unit
BC	Broad Component
CO	Carbon Monoxide, C≡O
CRIRES	CRyogenic InfraRed Echelle Spectrograph
ESO	European Space Observatory
FWHM	Full width at half-maximum
FWZI	Full width at zero intensity
HITRAN	High-resolution transmission molecular Absorption (https://hitran.org/)
IDE	Integrated development environment
IRTF	Infrared Telescope Facility
Jy	Jansky (unit of flux density)
LTE	Local Thermal Equilibrium
MIR	Mid-Infrared
μm	Micrometer, or micron (10^{-6} meters)
MMSN	Minimum Mass Solar Nebula
Myr	Million years
n_{13-30}	Spectral index between 13 μm and 30 μm

NC	Narrow component
NIR	Near-infrared
PMS	Pre-main-sequence
PPD	Protoplanetary disk
RD	Rotation diagram
SED	Spectral energy distribution
S/N	Signal-to-noise ratio
TTs	T-Tauri stars
VLT	Very Large Telescope

ABSTRACT

The inner radii ($<$ 10 AU) of protoplanetary disks (PPDs) are the birthplaces of exoplanets. Understanding what happens at these planet-forming distances requires the knowledge of inner gaseous disk evolution. Carbon monoxide (^{12}CO; hereafter CO) gas is known to be an effective tracer of excited molecular gas at small radii (0.01 AU – 10 AU). Therefore, in this work, the depletion of molecular gas is traced as the planet-forming regions of PPDs evolve and become gas-poor. To probe CO gas properties, a LTE (local thermal equilibrium) molecular excitation model is employed. Spectral emission of CO and H_2 (molecular hydrogen) gas are compared to analyze gas properties in both gas-rich, full disks and gas-poor transition disks. This approach demonstrates a radial stratification of molecular gas: CO lines are increasingly narrower than H_2 lines for disks with large inner gaps, or cavities, suggesting a recession of CO gas in the inner disk. In this thesis, I report results from an excitation analysis of CO spectra to identify how inner disk gas properties change as inner dust cavities form.

I. INTRODUCTION

Protoplanetary disks (PPDs) are rotating disks of circumstellar material (gas and dust) that coexist with a nascent star during its formation and evolution resulting in a mature planetary system like the Solar System. Supplying material to both the central protostar and upcoming protoplanets, PPDs dictate the evolution of both. Therefore, studying the planet forming regions in PPDs is crucial to understanding planet formation. In this thesis, analysis focuses on molecular gas emission spectra from the inner disk ($\lesssim$ 20 AU) of disks tracing the physical properties of the gas present as well as detecting the recession or depletion of molecular gas at small radii.

I.1 Protoplanetary Disks

The star formation process naturally produces PPDs as illustrated by figure 1. Vast nebulae incubate cold gases into dense filamentary structures which condense into warm cores. These cores of concentrated prestellar material are initially shrouded by an optically thick envelope of dust and gas. Under these conditions, the gravitational collapse of infalling materials conserves the net angular momentum of its natal cloud by settling into a rotating disk of dust and gas around the central protostar. The material remains in the disk as a reservoir for both star and planetesimal formation lasting anywhere from ~10^6 to $> 10^7$ years, thus imposing an upper time limit on the formation of a planetary system (Li et al. 2014).

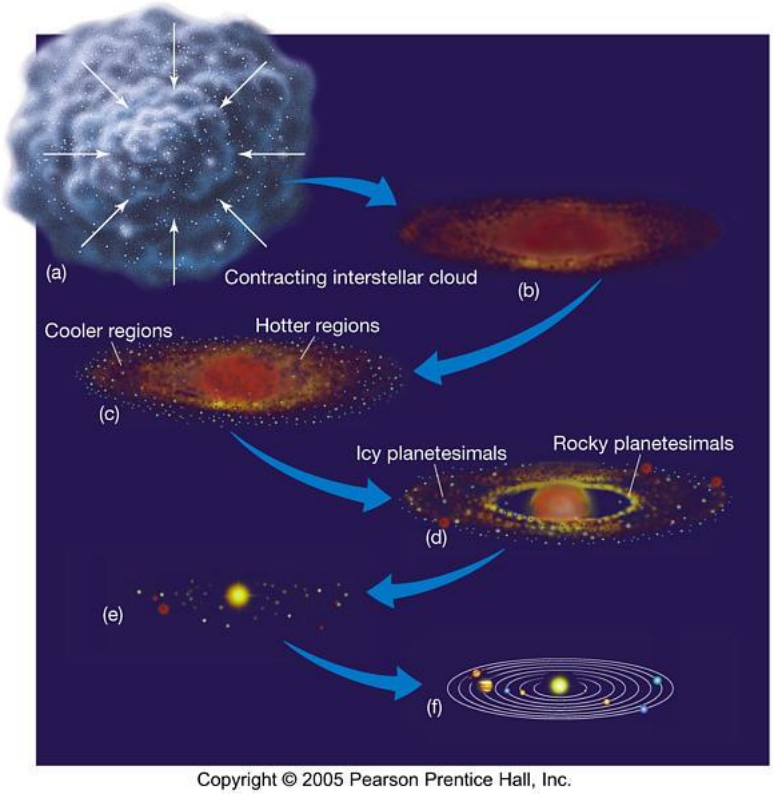

Figure 1. Cartoon of Solar System formation. (a) Nebular cloud collapse initiating star formation. (b) YSO material accretion and accumulation into a disk structure. (c) First stages of planet formation in the PPD. (d) Planetesimals form and grow due to PPD evolution. (e) Complete gas disk dissipation. (f) Final stage of planet formation.

Observational markers of disk presence are evident in emission from scattered light, the thermal continuum, and spectral lines (Andrews 2020). Scattered light emission is dominated by micron-sized dust grains, thus revealing the fine, dusty structural features throughout the disk (e.g., Waters 2015). Thermal emission comes from larger disk solids and spans the micron-to-centimeter continuum which helps to identify probable planet formation sites and signatures (e.g., Dutrey et al. 2014, Andrews et al. 2016). Both dust and disk solids contribute positively to the excess infrared emission observed in spectral energy distributions (SEDs) of YSOs (section I.1.1). Spectral emission lines are the rotational-vibrational transitions of excited molecular gases in the superficial atmosphere

of the PPD (e.g., Chiang and Goldreich 1997, Najita et al. 2003, Salyk et al. 2009, Brittain et al. 2009). Molecular spectra are used to make physical inferences about the radial temperature profile, column densities, and gas velocities. Signatures from accretion shocks, molecular outflows, jets, and effects of photoevaporation also contribute to molecular spectra. Figure 2 schematically displays the general structure of a PPD and emission origins in reference to their location in the disk.

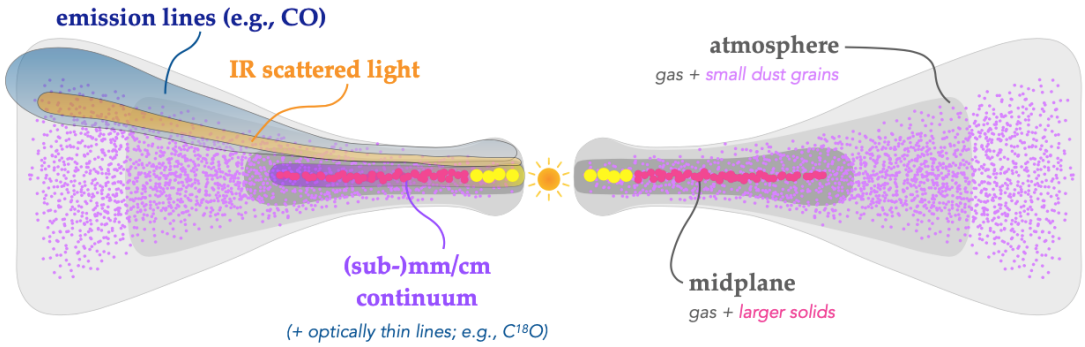

Figure 2. Anatomy of protoplanetary disk structure and observational regimes (not to scale). Disk gas is shown in grayscale and particles are represented as solid circles of varying sizes and colors (which denotes temperature difference, yellow being the warmest). On the left lobe are labeled the observational wavelength regimes associated with the emission source. The right lobe labels correspond to the physical structures that define radial and vertical disk composition. (*Source*: Andrews 2020).

The structure of PPDs is an observationally tested design which holds for a majority of disks around pre main sequence (PMS) stars. Angular momentum transport and stellar irradiation fundamentally and energetically set the stage for PPD structure and dynamics. Stellar accretion brings circumstellar material inward while photoevaporation depletes the inner disk. Under these conditions, other evolutionary processes also interact with inner disk material: protostellar outflows and jets (Herczeg et al. 2011, Banzatti et al. 2015a) coupled with magnetohydrodynamic (MHD) winds (Ercolano and Pascucci

2017). Inner PPD physics reveal their influence through characteristic spectral features visible in emission line profiles (see Section I.2.2). Moreover, the inner disk nurtures planet formation insinuating planet-disk interactions are frequent in PPD evolution.

Protoplanetary chemistry and dynamics are fueled, in part, by intense radiation close to the star. At larger radii, however lower temperatures and densities prevail, contrasting the optically thick, warmer inner disk. Molecular species are found in their gaseous form until they undergo deposition in the outer disk, ultimately influencing planetesimal growth and global disk turbulence, if disk viscosity allows (Pontoppidan et al. 2014, Turner et al. 2014). Prevailing energy transport mechanisms include molecule-particle collisions, disk viscosity, hydrodynamic turbulence, magnetorotational instabilities (MRI), and grain growth and migration (Testi et al. 2014 and references therein). External factors such as dynamic disruptions from flyby stars and photoevaporation from nearby stars can also strip material from PPD systems (commonly occurs in binaries and situations in which flyby encounters are possible, see Alexander et al. 2014).

A PPD will evolve by accreting material on the central star or dynamic clearing by planet growth. The relationship shared between PPDs and planets cannot yet be fully understood without imposing constraints. Furthermore, imaging the inner disk of PPDs requires high spectral and spatial resolution to investigate the planet-forming regions of PPDs (figure 3).

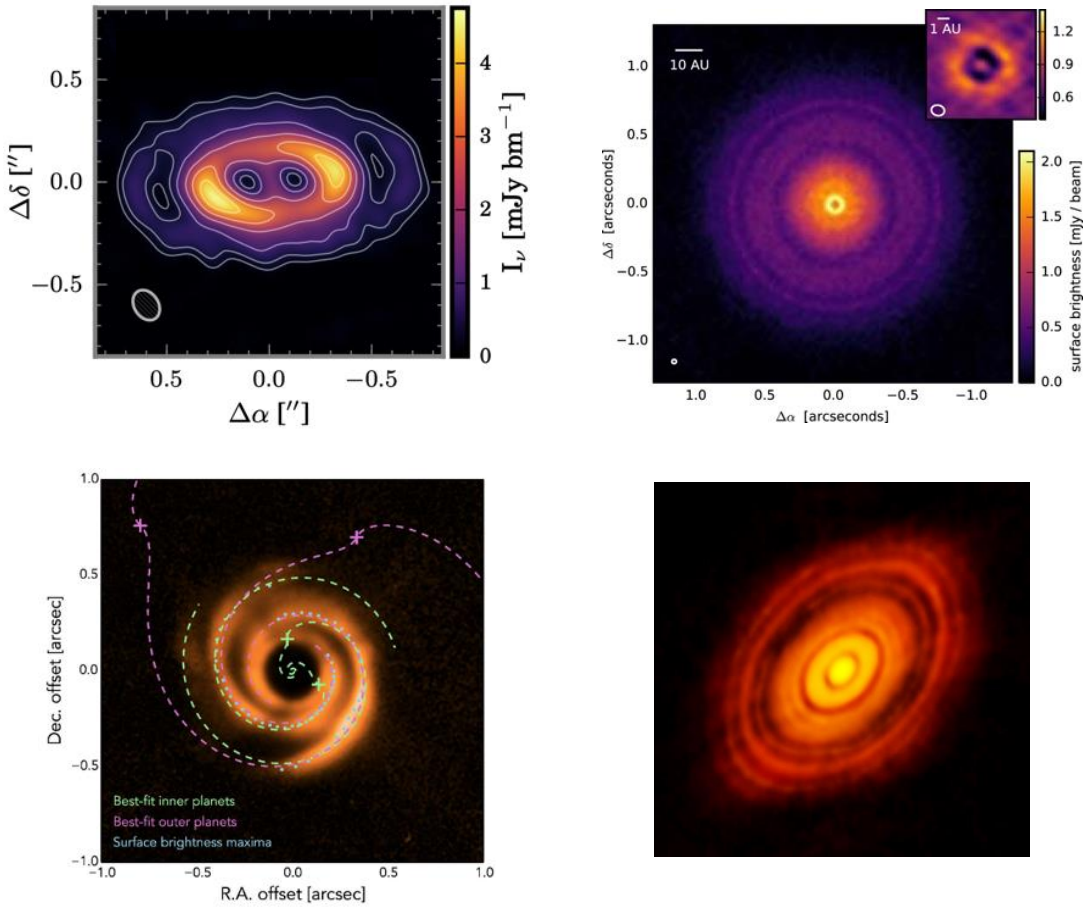

Figure 3. Diverse continuum emission from four PPDs. Three of these disks pertain to the sample analyzed in this work (AA Tau, TW Hya, and HD 135344b). *Upper left:* AA Tau (Loomis et al. 2017). *Upper right:* 870 μm TW Hya (Andrews et al. 2016). *Lower left:* 1.245 μm HD 135344b (Stolker et al. 2016). *Lower right:* 1.3 mm HL Tau (ALMA Partnership et al. 2015).

I.1.1 *Evolution of Inner Disks*

Stellar accretion, planetesimal growth, planet clearing, photoevaporation, and MHD winds contribute to inner disk evolution and consequently inner disk observations. A common observational characteristic of evolved, or evolving, disks is suggested as the development of inner gaps found in the dust continuum – categorized by n_{13-31}. In fact, a harbinger of disk evolution is often interpreted as inner gap detection (Banzatti et al. 2015; 2020, Pontoppidan et al. 2008; Francis and van der Marel 2020) and outer disk mass loss in some cases (van der Marel et al. 2019). Dissipation of the inner disk – as opposed to its ongoing evolution –is further investigated through molecular spectra in the

mm continuum dust cavity (Salyk et al. 2007a, Pontoppidan et al. 2008, Hoadley et al. 2015, Banzatti and Pontoppidan 2015).

The first instance of an SED classification scheme for YSOs was developed in 1984 by Lada and Wilking in which the infrared index was determined through the excess or absence of IR emission at smaller micron wavelengths. The spectral index, α_{IR}, is the mathematical slope between two wavelengths in stellar SED, specifically from 1 μm to ~20 μm (figure 4). YSOs are classified as Class 0, Class I, flat spectrum, Class II, and Class III by their SED slope as defined by Lada and Wilking (1984):

$$\alpha_{\mathrm{IR}} = \frac{d \log \nu F_{\nu}}{d \log \nu} = \frac{d \log \lambda F_{\lambda}}{d \log \lambda}$$

Class 0 sources ($\alpha_{\mathrm{IR}} < -0.3$) are completely embedded stellar objects with emission predominantly in the far IR and none in the NIR and MIR emission. Class I sources have shed the envelope of material shrouding the protostellar core and thusly $\alpha_{\mathrm{IR}} > 0.3$ due to the lack of material obscuring the light emanating from the central core. Flat spectrum sources then have a slope close to zero ($-0.3 < \alpha_{\mathrm{IR}} < 0.3$) as the SED continues to emerge from a hotter object. Class II sources are completely unshrouded YSOs with a defined PPD, suitable for planet formation with an index between -1.6 and -0.3. Finally, Class III sources ($\alpha_{\mathrm{IR}} < -1.6$) indicate sources that are in the final stages of formation with a gas- and dust-poor debris disk (Boss and York 1996, review by Armitage 2020).

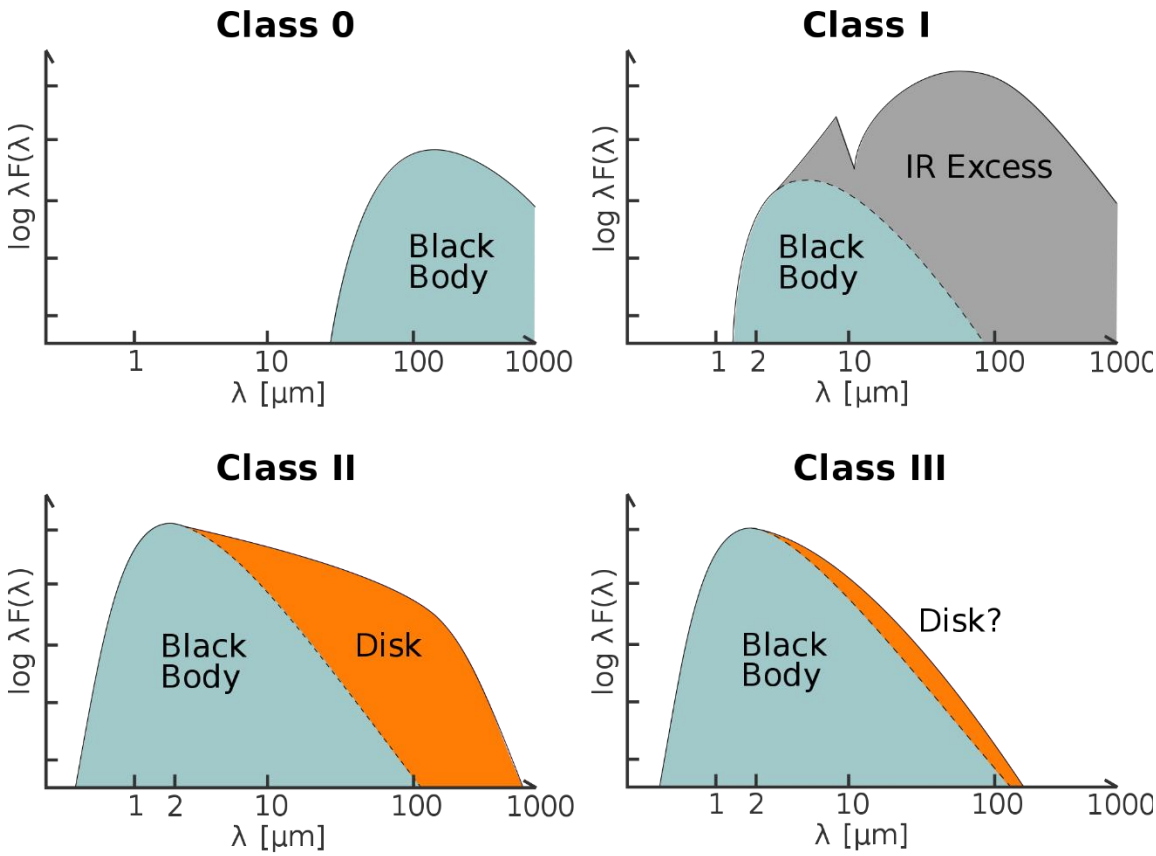

Figure 4. Spectral energy distributions of YSO (young stellar object) classification by infrared index (α_{IR}). (credit: Turck-Chieze 2011)

Class II YSOs are of particular interest because this is where a star spends most of its formative years, according to sample statistics of YSO clusters (Andrews et al. 2014). Therefore, there have been extensive studies done on diverse samples of Class II objects in various protoplanetary stages that present emission signatures in infrared molecular spectroscopy of the excited gas emanating from the planet-forming regions of the PPD (Najita et al. 2003, Pontoppidan et al. 2008, Banzatti et al. 2020). Looking closer, the SED at these wavelengths gauges star forming progress, but lacks the precision in isolating disk evolution. Because global and local changes indiscriminately contribute to the SED, any analyses are incomplete, at best. Information about inner gas disk properties comes from high resolution spatial and spectral observations using radio

interferometry and spectroscopy.

The infrared index is a more sensitive tracer of disk characteristics as opposed to broad evolutionary steps of a pre-main sequence star. Large samples of PPDs are used to infer/speculate a theoretical timeline associated with disk dispersal and planet formation. Young PPDs are considered gas-rich, or "full" disks. Conversely, PPDs displaying a central hole or gap in the dust emission earn the classification of "transition" disk (Espaillat et al. 2014). The term refers to the transitional phase between a "full" disk and the gas- and dust-poor debris disk. This age range is characterized by its infrared index between 13 μm and 31 μm (n_{13-31}) in the SED of the YSO:

$$n_{13-31} = \frac{\log(\lambda_{31}F_{\lambda_{31}}) - \log(\lambda_{13}F_{\lambda_{13}})}{\log(\lambda_{31}) - \log(\lambda_{13})}.$$

Used by Furlan et al. (2006, 2009) and Brown et al. (2007), to track dust settling in disk layers and the absence of warm μm dust in PPDs, the infrared index is sensitive to the amount and radial distribution of hot dust in the inner disk. This classification scheme came to fruition in terms of PPD evolution after the infrared index empirically showed the capacity to effectively distinguish between full disks and disks with a cavity. It is worth noting the value of the infrared index varies with disk geometry. Figure 5 illustrates the physical differences between values of n_{13-31} in the SEDs for full disks and those with cavities (Appendix D in Banzatti et al. 2020).

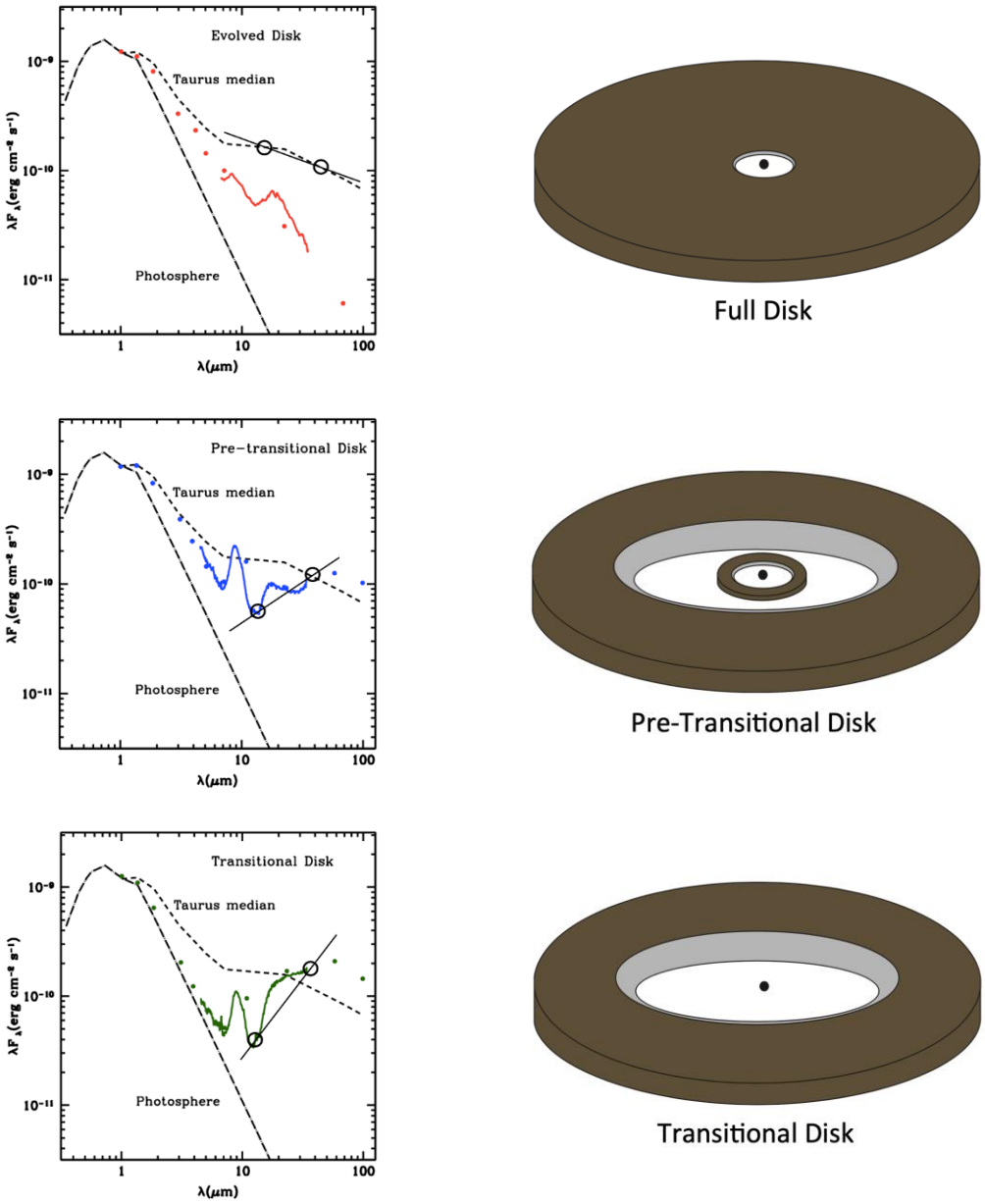

Figure 5. Spectral energy distributions (SEDs) and corresponding illustrations of dust emission for full, pre-transitional, and transition disks. The slope of the spectral index, n_{13-31}, is shown in each plot as a black solid line intersecting two open circles located at roughly λ = 13 μm and λ = 31 μm. The Taurus median – labeled as dashed line – signifies the median value of transition disk SEDs in the Taurus star-forming region. The stellar photosphere is also labeled as a dashed dotted line. The SEDs (in order) belong to RECX 11, LkCa 15, and GM Aur, from top to bottom (Adapted from Espaillat et al. 2014, 499)

I.2 Molecular Emission Spectra from Protoplanetary Disks

While PPD observations are plentiful at large radii in the mm continuum (Andrews 2020, Dutrey et al. 2014), the focus of this thesis makes use of the spectral line emission observations from warm gases at small disk radii. Particle collisions and stellar irradiation dominate warm molecular gas emission thus making spectroscopy a powerful tool to observe warm/hot gas in PPDs (Najita et al. 2003, Salyk et al. 2009; 2011, Banzatti & Pontoppidan 2015). The continuous bombardment of stellar radiation excites molecular gases held under pressure in PPDs, sculpting the rovibrational spectra from inner disks. A wealth of molecular gas is found throughout PPDs tracing the radial and vertical profile of the PPD structure, thus observing molecular transitions permits constraints to be placed on emitting gas properties (Carmona 2008). Many chemically simple molecules across several magnitudes of wavelength have been investigated in PPDs, some of which are shown in Table 1 (Dutrey et al. 1997; Kastner et al. 1997; Thi et al. 2004; Chapillon et al. 2012b; Qi et al. 2013a; Bergin et al. 2010).

Table 1. Detected molecular species, their transitions, and properties probed in the millimeter/sub-millimeter ranges.

Molecule	Transitions	Quantity	Wavelengths
^{12}CO, ^{13}CO	Rotational and Ro-vibrational	Temperature	IR, FIR, sub-mm/mm
H_2	Ro-vibrational	Temperature	IR
CS, H_2CO, HC_3N	Rotational	Density	sub-mm/mm
HCO^+, N_2H^+, CH^+	Rotational	Ionization	sub-mm/mm, FIR
CN, HCN, HNC	Rotational	Photochemistry	sub-mm/mm
H_2O, OH (inner disc)	Rotational	Temperature Photochemistry	IR
H_2O, OH (outer disc)	Rotational	Photodesorption	FIR
Complex organics (outer disc)	Rotational	Grain surface processes	sub-mm/mm
Complex organics (inner disc)	(Ro-)vibrational	High-T chemistry Photochemistry	IR
HD, DCO^+, DCN, H_2D^+	Rotational	Deuteration	FIR, sub-mm/mm
CS, HC_3N	Rotational	Turbulence	sub-mm/mm

Source: Table from Dutrey et al. 2014.

I.2.1 *Excitation*

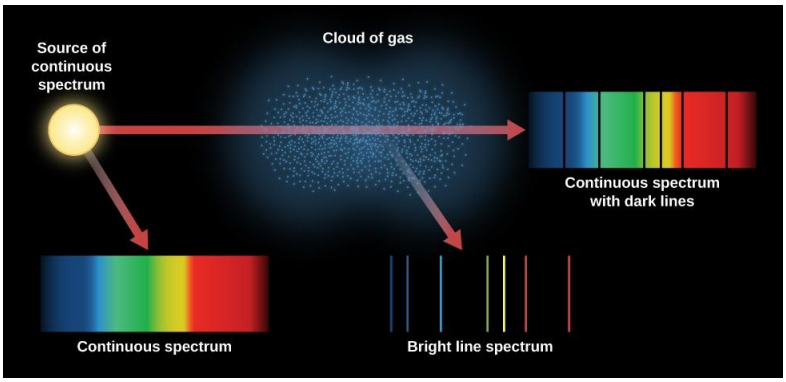

Figure 6. Cartoon of the different types of spectra. Absorption spectra appear as dark lines in continuum emission. Emission spectra appear as bright lines in an otherwise dark spectrum. (Credit: Andrew Fraknoi, David Morrison, Sidney C. Wolff, OpenStax Astronomy https://openstax.org/books/astronomy/pages/5-5-formation-of-spectral-lines)

Molecular emission spectra are a result of quantum mechanical phenomena pertaining to the interaction between radiation and matter (figure 6). Specifically, for PPDs, this interaction is between molecules and stellar radiation. It is understood through quantum mechanics that molecules do not access continuous values of internal energy, but instead a discrete range of energy levels spaced out by their molecular geometry (figure 7). When a molecule gains the exact energy required to transition from a lower energy level to a higher energy (excitation), the molecule will spontaneously lose the gained energy in the form of an emitted photon with a frequency determined by the change in energy:

$$\Delta E = \left|E_{upper} - E_{lower}\right| = hf_{emit},$$

where E_{upper} is the upper-level energy of the transition, E_{lower} is the lower-level energy of the transition, f_{emit} is the frequency of the emitted photon, and h is Planck's constant. Within a transition, a photon is either emitted, if the transition is from an upper-level state

to a lower-level, or absorbed, if the transition is from a lower state to an upper state (figure 6).

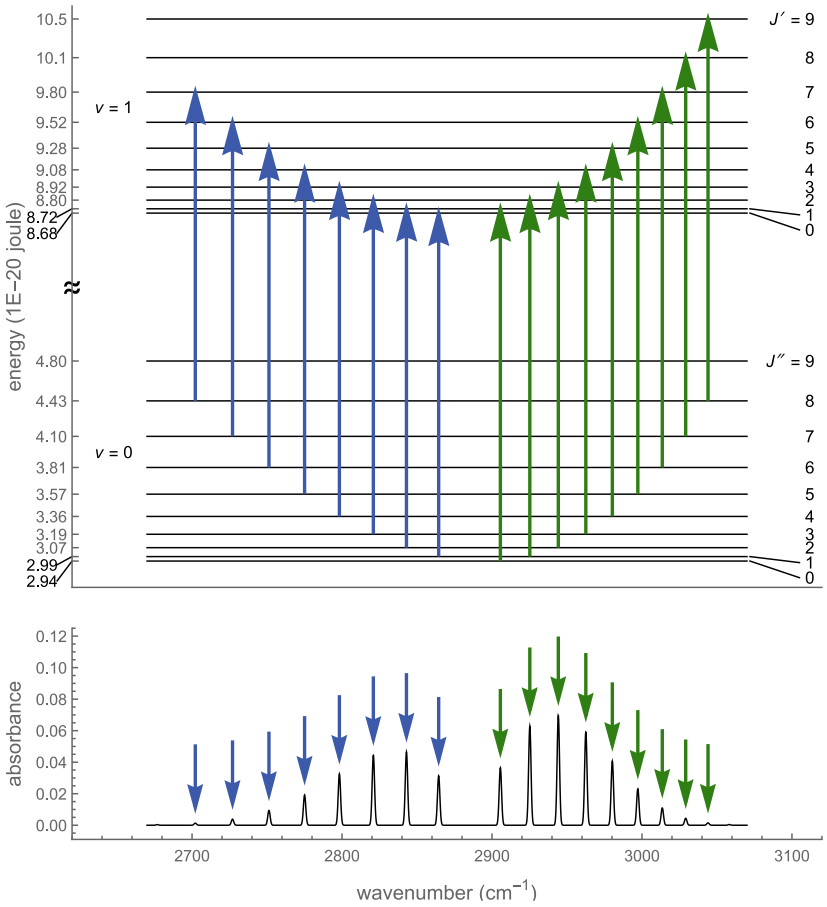

Figure 7. Energy ladder and rovibrational absorption spectrum with transitions marked with blue arrows (P-branch) and green arrows (R-branch). (Source code credit: Whitney R. Hess and Lisa M. Goss from Idaho State University).

Nevertheless, the principle is the same for either transition in that the exchange of energy is equal between the environment and molecule. According to the Born-Oppenheimer approximation, total molecular energy may be deconstructed as a linear combination of independent energy modes. In order from smallest in energy to largest, those contributions are rotational, vibrational, and electronic:

$$\Delta E = E_{rot} + E_{vib} + E_e$$

Hence, rotational-vibrational (rovibrational) spectra display the coupled rotational and vibrational transitions within a single electronic energy level. Because the central star continuously emits radiation, molecules reemit the energy as scattered photons which populate rovibrational energy levels constructing the familiar molecular spectral lines (figure 7). Rotational energy levels are usually denoted by the quantum number associated with the angular momentum of the molecule: $J = 0, 1, 2,\ldots$ for ground and subsequent excited states, and vibrational energy levels are denoted by $v = 0, 1, 2,\ldots$ for ground and excitations. For purely rotational transitions, the allowed transitions are $\Delta J = J'' - J' = \pm 1, 0$ where the double primed number denotes the upper-level energy and the single prime for lower-level energy levels. Vibrational transitions differ in that they assume a change in J for a change in v – where the allowed transitions are $\Delta v = v'' - v' = \pm 1, 0$ – due to the larger amount of energy needed for a vibrational transition. For $\Delta J = +1$, the R-branch arises; likewise, for $\Delta J = -1$, the P-branch appears. Furthermore, the vibrational transition from the first excited state to the ground state ($v = 1\text{-}0$) is known as the fundamental transition while every transition with a greater upper-level energy is called overtone emission ($\Delta v = 2$ e.g., $v = 2\text{-}0$).

I.2.2 *Kinematics*

Gas kinematics determine the observed shape of molecular emission line profiles. A disk of emitting gas in Keplerian rotation produces a characteristic double-peaked emission profile (figure 8). This double-peaked feature is resolved as a single peak at low disk inclinations. Double-peaked profiles are rather infrequent among PPD emission profiles (e.g., Brown et al. 2013, Banzatti and Pontoppidan 2015, Salyk et al. 2009, Bast et al. 2011). Emission line widths trace the Keplerian velocity of the emitting gas.

Narrow features rise from slower moving gas in highly inclined disks, while broad emission features indicate higher velocity gas. Assuming Keplerian motion, slower velocity corresponds to larger radii, while higher velocities to smaller radii following Kepler's Law:

$$FWHM_{CO} = 2 \sin i \sqrt{\frac{GM_*}{R_{CO}}}.$$

The quantity i represents the inclination of the disk, G is the gravitational constant, M_* is the stellar mass, and R_{CO} is the inner radius of the CO gas.

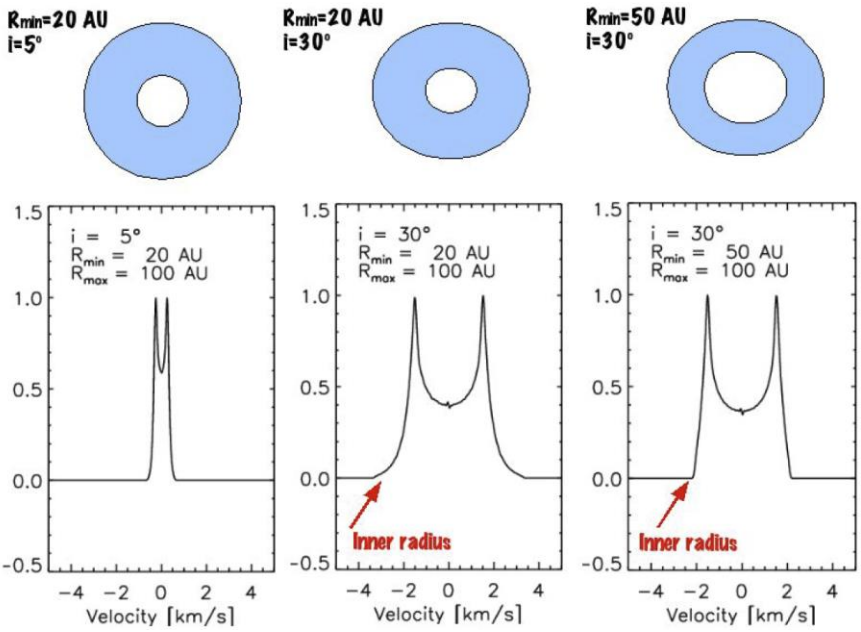

Figure 8. Emission line shape of gas disk in Keplerian rotation as a function of inclination and inner disk distance. (*Source*: Carmona 2009)

Furthermore, line profile shapes are also defined by the degree of depletion of inner disk gas. Figure 9 illustrates four hypothetical conditions that produce significant emission line profiles as well as the velocity and spatial distribution of the emitting gas (Brittain et al. 2009). Gas close to the central star will emit a broader profile, however

the distribution of the emitting gas sets apart the environmental conditions.

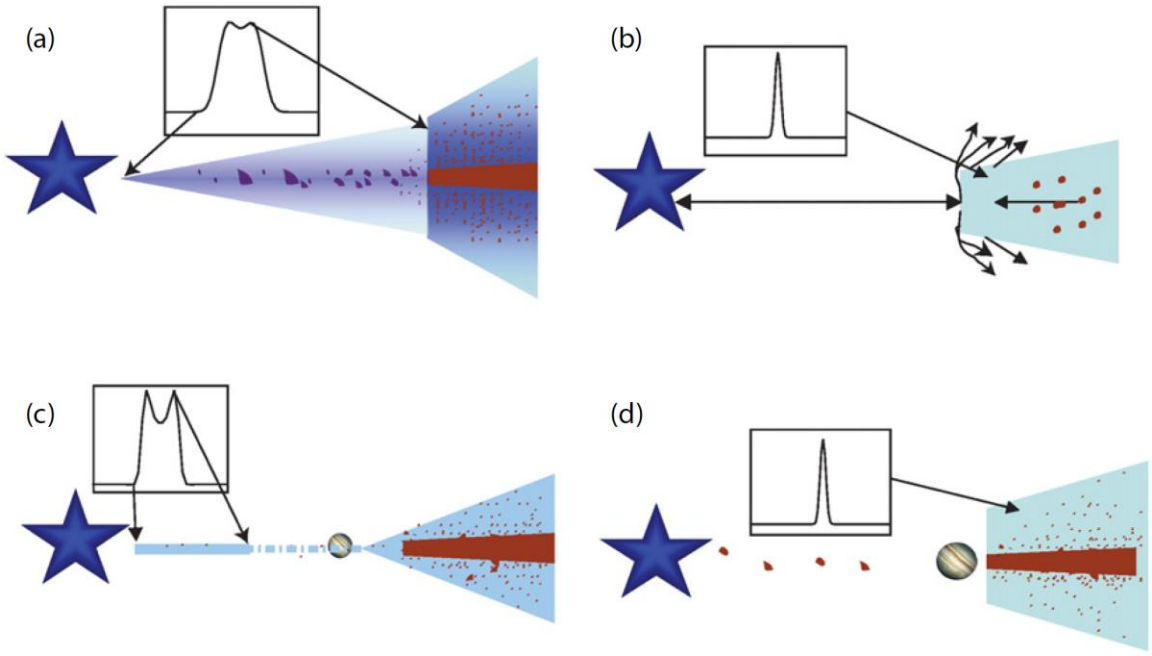

Figure 9. Inner gas disk emission line shape in the absence of dust emission in the inner disk. Coupled with millimeter observations, potential scenarios for gas emission can be inferred. (a) Emission of gas from the inner disk. (b) Gas emission retreated from inner disk. (c) Giant gas giant resulting in inner disk gas emission. (d) Giant gas giant causes emission mimicking that of (b). (*Source*: Brittain et al. 2009).

I.2.3 *Carbon Monoxide Gas in Inner Disks*

Of the molecular species present in inner disks, CO is ubiquitous across large samples of PPDs (Najita et al. 2003, 2007, Salyk et al. 2011, Banzatti and Pontoppidan 2015). Molecular hydrogen (H_2) is more abundant than CO by 4 orders of magnitude (France et al. 2014), but is cruelly difficult to observe since it lacks a permanent electric dipole. On the other hand, CO is a spectrally expressive molecule, as expected from the associated Einstein coefficients (section I.2.4), producing a rovibrational spectrum from the warm gas in the inner disk region of PPDs. Although rovibrational H_2 spectra observations are possible in the hot disk atmosphere via far-UV, CO is still used as a proxy of gas mass for inner disk regions (Salyk et al. 2009; 2011, Banzatti and Pontoppidan 2015, Herczeg et al. 2011).

Rovibrational CO is efficiently excited in the warm, planet-forming conditions of the inner disk. Rotational temperatures (section I.2.4) of CO gas range between 10^2 K and 10^3 K within inner dust cavities of PPDs. The surface layer is observed most easily because it is optically thin and directly exposed to stellar irradiation as opposed to the shielded interior layers (Chiang and Goldreich 1997). Temperature of the emitting gas can be deduced from emission line ratios, gas mass and column densities assuming the gas is optically thin, and dynamics of the emitting area of gas. Interpretations of molecular spectra, however are fundamentally incomplete due to assumptions regarding local thermal equilibrium (LTE), opacity, relative populations of molecules, and disk properties (Carmona 2008).

Various factors contribute to the diversity in CO emission line profiles (figure 10) including disk winds (Ercolano and Pascucci 2017), outer disk atmosphere absorption, molecular outflows, and high extinction from foreground molecular clouds (Brown et al. 2013).

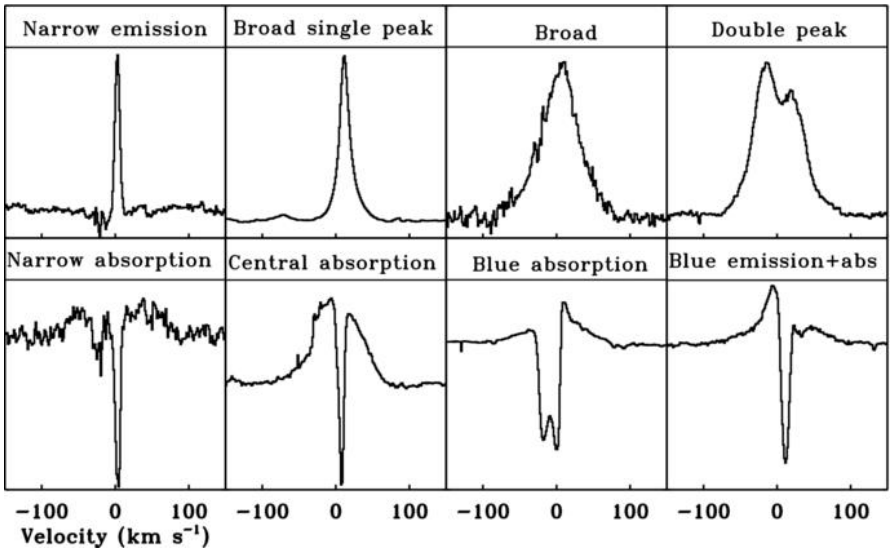

Figure 10. Variety of emission and absorption molecular velocity line profiles for CO. (*Source*: Brown et al. 2013).

I.2.4 *Description of Rotation Diagram Technique*

Rotation diagrams (RDs), also known as a population diagram or excitation diagram, graphically present physical properties causing excited molecular gases from emission lines. Use of this analytical tool has become commonplace in PPD molecular spectroscopy due mostly to the sensitivity to LTE conditions in the gas, opacity, and gas temperature.

Generating a RD requires the integrated line fluxes of the vibrational emission lines in a spectrum and their rest wavelengths. The y-axis is a function of the transition line flux, F_ν, and transition frequency, ν:

$$Y(F_\nu) = \ln\left(\frac{4\pi F_\nu}{h\nu A_{ul} g_{ul}}\right). \quad \text{(I.a)}$$

The denominator is a product of the Einstein coefficient of spontaneous emission for the upper and lower energy states, A_{ul}, statistical weight of the transition, g_{ul}, the frequency of the transition, ν, and Planck's constant (Goldsmith and Langer 1999). Essentially, the Einstein coefficient is proportional to the likelihood of spontaneous emission per unit of time; hence the unit s^{-1}. The statistical weight is the degeneracy of a given state for a given rotational quantum number: $g = 2J + 1$ (Šimečková et al. 2005).

The x-axis is then a function of the transition frequency, which corresponds to an upper-level energy, E_{up}. This value is divided by the Boltzmann constant, k_B, to compose the x-axis:

$$X(\nu) = \frac{E_{up}}{k_B}. \quad \text{(I.b)}$$

Under LTE conditions, rotation diagrams can yield reasonable estimates for excitation temperatures and column density as long as CO emission is optically thin and

the energy levels are thermally populated (Goldsmith and Langer 1999). In LTE conditions,

$$Y(F_\nu) \propto e^{-E_u/k_B T_e}$$

Therefore,

$$\frac{d}{dE_u}\ln\big(Y(F_\nu)\big) = \frac{-1}{k_B T_e}$$

In this case, the excitation temperature is proportional to the slope of the RD by $-1/T_e$ and the column density can be assumed to be the column density of the molecule as a whole (Najita et al. 2003; Goldsmith and Langer 1999).

When these assumptions are not secure, the RD reflects a change in physical dynamics (figure 11). For example, in optically thick conditions the function in equation (I.a) instead curves sharply at lower frequencies and then gradually at higher frequencies, although other mechanisms can produce this curvature – including temperature gradients and nonthermal excitation of transitions. In figure 11, differences in optical thickness and temperature are displayed by holding a single value of column density or temperature fixed while varying the other. The emitting area scales proportionally with the absolute fluxes of all the lines in this simple model and are therefore omitted here. The most constraining property of line flux measurement is the relative flux between lines in a single spectrum. This ratio is sensitive to the excitation temperature and column density of the emitting gas; consequently, the line flux ratios among rovibrational branches affect RD curvature.

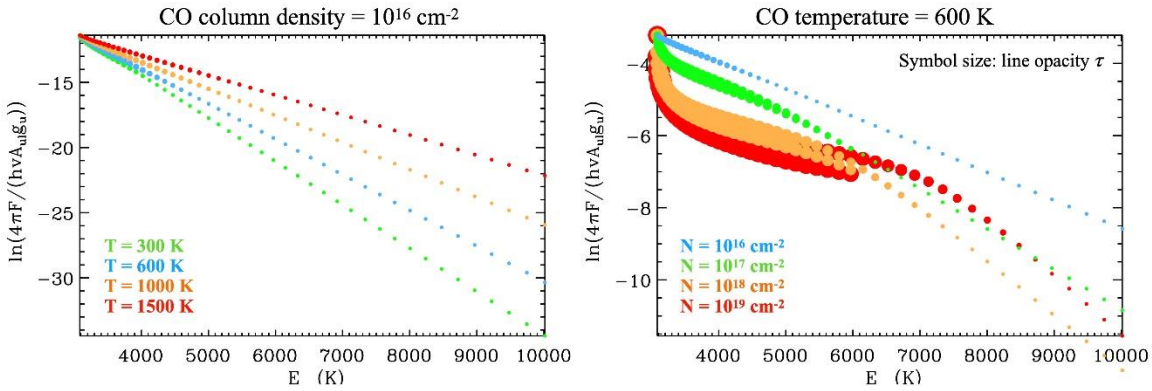
CO column density = 10^16 cm^-2
ln(4πF/(hνA_ul g_u))
T = 300 K
T = 600 K
T = 1000 K
T = 1500 K
E (K)
CO temperature = 600 K
Symbol size: line opacity τ
N = 10^16 cm^-2
N = 10^17 cm^-2
N = 10^18 cm^-2
N = 10^19 cm^-2
E (K)

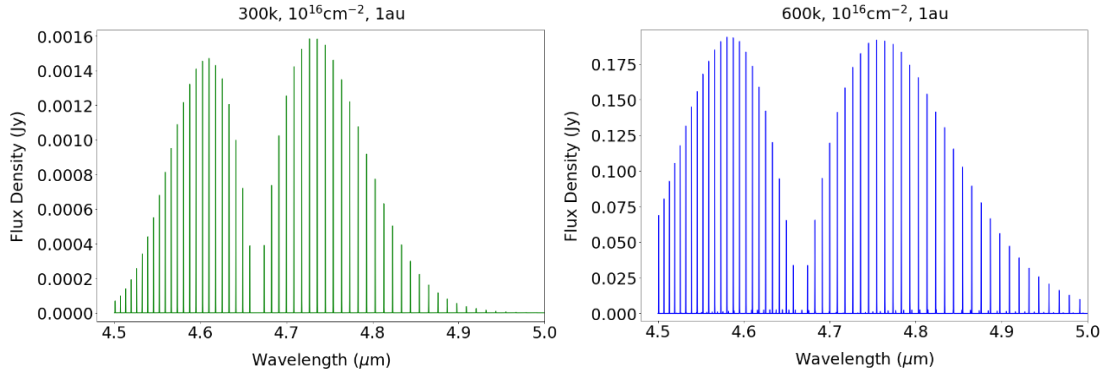
300k, 10^16cm^-2, 1au
Flux Density (Jy)
Wavelength (μm)
600k, 10^16cm^-2, 1au
Flux Density (Jy)
Wavelength (μm)

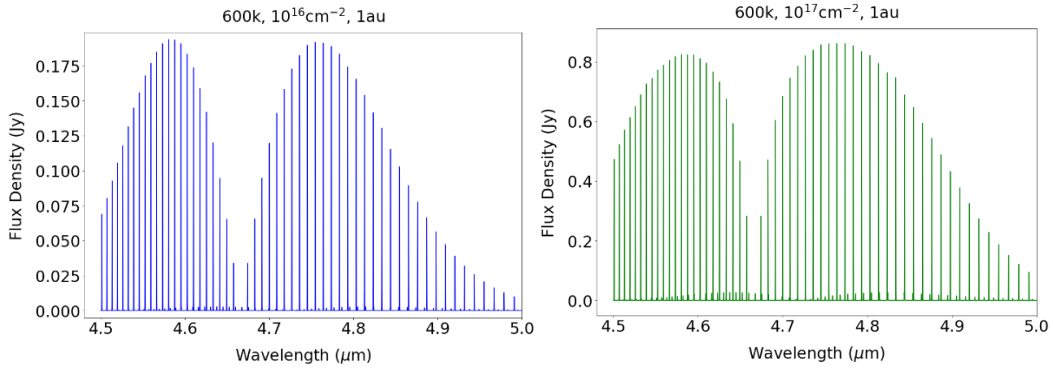
600k, 10^16cm^-2, 1au
Flux Density (Jy)
Wavelength (μm)
600k, 10^17cm^-2, 1au
Flux Density (Jy)
Wavelength (μm)

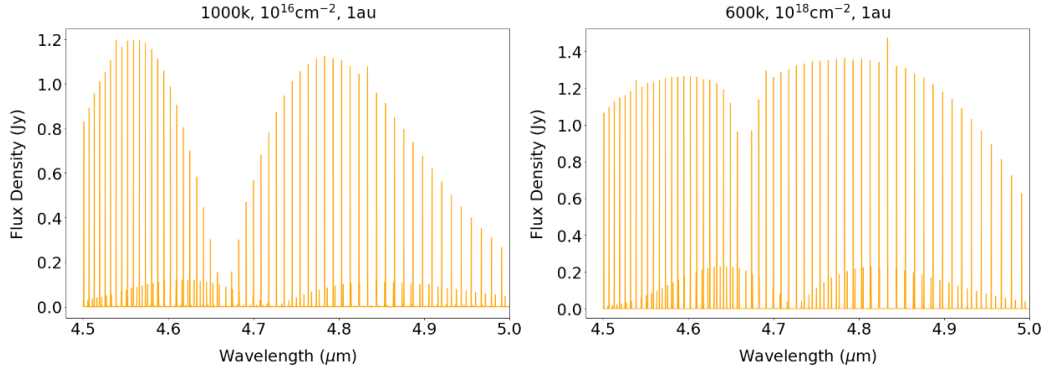
1000k, 10^16cm^-2, 1au
Flux Density (Jy)
Wavelength (μm)
600k, 10^18cm^-2, 1au
Flux Density (Jy)
Wavelength (μm)

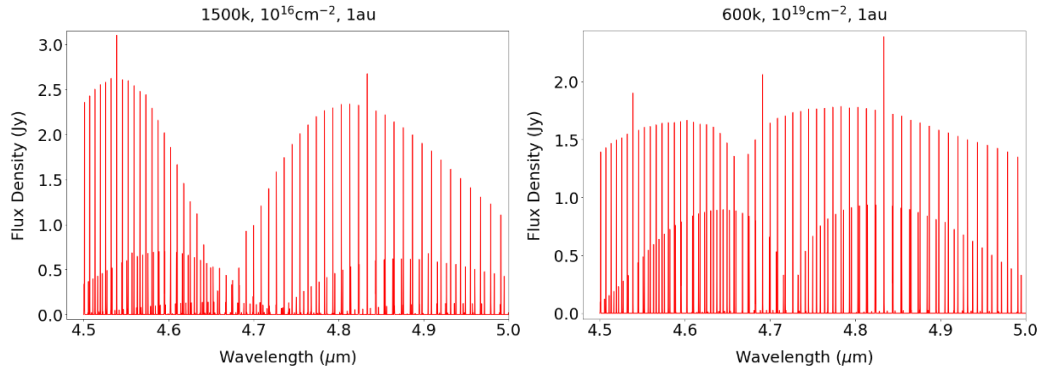

Figure 11. Illustration of rotation diagram technique applied to synthetic CO line fluxes from spectra of varying temperatures and column densities. *Top right:* RD demonstrates 4 isothermal curves with a constant column density. *Top left:* RD shows an isothermal spectrum with 4 different column densities. Thicker line opacities produce a noticeable curve in the rotation diagram. Below the RDs are molecular CO rovibrational spectra from which they are created. The colors correspond to the rotation diagrams above – from top to bottom, the left column increases in temperature and the right column increases in column density. All spectra are normalized to the strongest line flux in each figure, for visualization purposes. Model used in these figures is the one described in section (III.3).

I.3 Spectral Sample of 15 Protoplanetary Disks

Table 2. Sample properties. CO ranges are measured from the data.

Star Name	M_*	L_*	$\log L_{acc}$	n_{13-31}	Dust cavity (AU)	CO range (μm)
DF Tau	0.6	0.6	-0.63	-1.09	…	4.64-4.77 (P3-P11)
RU Lup	0.55	1.45	-0.01	-0.53	…	4.65-4.98 (P1-P30)
AA Tau	0.6	0.5	-1.43	-0.36	28	4.65-4.90 (P1-P24)
DR Tau	0.93	0.63	-0.24	-0.34	…	4.64-4.99 (P2-P32)
HD 144432S	1.7	14.8	-0.35	-0.28	…	4.64-4.77 (P1-P11)
CV Cha	2.1	8	-0.41	-0.23	…	4.65-4.99 (P2-P32)
TW Cha	1.0	0.38	-1.66	-0.16	…	4.73-4.99 (P1-P14)
EX Lup	0.5	1.1	-1.3	-0.14	…	4.66-4.89 (P1-P23)
HD 139614	1.5	6.6	-0.1	0.72	6	4.71-4.82 (P6-P15)
Do Ar 44	1.22	0.93	-0.73	0.8	34	4.64-4.77 (P1-P11)
HD 36112	1.56	11	-0.1	0.82	62	4.55-5.15 (P1-P47)
RY Lup	1.127	1.82	-1.4	0.87	68	4.65-4.98 (P1-P30)
TW Hya	0.61	0.23	-1.53	0.96	2.4	4.59-4.81 (P1-P14)
HD 142527	2	16.3	0.8	1.02	120	4.65-4.9 (P1-P23)
HD 135344B	1.43	6.17	-1.11	1.85	62	4.65-4.99 (P2-P32)

Source: Data from Allen et al. 2017; Andrews et al. 2016; Fairlamb et al. 2015; Fang et al. 2018; Francis et al. 2020; Furlan et al. 2009; Herczeg and Hillenbrand 2014; Ingleby et al. 2013; Long et al. 2019; Maaskant et al. 2014; Manara et al. 2016; Menu et al. 2015; Mendigutía et al. 2014; Pascucci et al. 2016; Pinilla et al. 2018; Salyk et al. 2013; Vioque et al. 2018.

Using the Cryogenic Infrared Echelle Spectrometer (CRIRES) from the Very Large Telescope (VLT) within the European Southern Observatory (ESO), rovibrational CO spectra (resolving power R~75,000) of 14 protoplanetary disks were obtained. One more spectrum was observed with a 1.1-5.3 μm high spectral resolution spectrograph (iSHELL) from the NASA Infrared Telescope facility (IRTF) with a resolving power of ~10^5. Sample stellar and disk properties along with the spectral range collected from each disk are listed in table 2.

I.3.1 *Description*

The sample spans a broad range of protoplanetary and demographic properties. The 15 spectra hail from various star forming regions (in no particular order): Taurus, Chameleon, Lupus, Hydra, Centaurus, and Scorpius. The fundamental rovibrational spectra of CO for 15 disks were collected; 53% of which have inner dust cavities detected from sub-mm dust continuum observations whereas the remaining 47% do not.

Emission profiles throughout the sample are single-peaked with the exception of AA Tau, CV Cha, and RY Lup which have an absorption component. Spectral coverage among the sample is not equal with the largest spectral range being 0.6 μm and the smallest 0.11 μm.

I.3.2 *Significance*

The sample captures a broad range in properties, from T-Tauri stars ($< 2M_{\odot}$) and Herbig Ae stars (2-8$M_{\odot}$) to gas-rich and transitional disks. Moreover, the sample contains a varied set of values for n_{13-31} corresponding to cavity presence. These data lend credence to their analysis due to their relative diversity in stellar and PPD properties. Of particular note in this sample is also the combination between the lack of knowledge

toward inner disk gas depletion and collection of high-resolution spectra.

II. GAS EVOLUTION IN INNER DISK CAVITIES FROM A SYNERGIC ANALYSIS OF IR-CO AND UV-H_2 SPECTRA

This chapter is based on a note by Sánchez et al. published to the *Research Notes of the American Astronomical Society* (RNAAS) vol. 5, no. 4 (2021).

II.1 Introduction

While ALMA observations reveal protoplanetary disk structures at > 10 AU in great detail (e.g., Andrews 2020), the best probe of inner disk gas at < 10 AU is high resolution spectroscopy at infrared (IR) and ultraviolet (UV) wavelengths. Warm (T > 500 K) H_2 can be observed at near- and mid-infrared wavelengths using ground-based spectrographs, with low detection rates (Bitner et al. 2008; Gangi et al. 2020). Hot (T > 1500 K) H_2 has been observed in a sample of ∼30 disks in the far-ultraviolet using the Cosmic Origins Spectrograph (COS) and the Space Telescope Imaging Spectrograph (STIS) on the Hubble Space Telescope (France et al.2012; Hoadley et al. 2015). The CO molecule is less abundant than H_2 by ~ 10^4, but it is an extremely effective tracer of gas in disks. Rovibrational CO spectra at NIR wavelengths probe gas at temperatures of ~300 – 1500 K and have been observed in hundreds of disks with a suite of spectrographs (e.g., Najita et al. 2003; Brittain et al. 2007; Pontoppidan et al. 2011; Salyk et al. 2011; Brown et al. 2013; Banzatti et al. 2018). Both IR-CO and UV-H_2 spectra have been identified as tracers of inner disk evolution, where emission line profiles shrink in velocity (i.e., reflecting a lower Keplerian velocity at larger disk radii) with the depletion of inner disk dust (Banzatti & Pontoppidan 2015; Hoadley et al. 2015). The relative

distribution of H_2 and CO in the inner dust cavity of one disk, RY Lup, has been studied by Arulanantham et al. (2018). In this work, we combine for the first time these molecular tracers for a sample of 15 protoplanetary disks spanning a range in evolutionary phases. The ultimate goal of this program is to study inner disk evolution to test models of planet formation and wind dispersal (e.g., Ercolano & Pascucci 2017).

II.2 Sample & Data

The sample includes 15 disks around T Tauri and Herbig stars, which were selected from previous works to trace a range of phases in inner disk depletion from dust and gas (AA Tau, CV Cha, DF Tau, DoAr 44, DR Tau, EX Lup, RU Lup, RY Lup, TW Cha, TW Hya, HD 135344B, HD 144432, HD 142527, MWC 758, HD 139614). The H_2 spectra for this sample come from France et al. (2012), Hoadley et al. (2015), and a new HST-COS program (GO-14703, PI: Banzatti) that was requested for this analysis (providing half of the sample). The CO spectra come from Pontoppidan et al. (2011), using VLT-CRIRES (Kaeufl et al. 2004), and Banzatti et al. (2018), using IRTF-iSHELL (Rayner et al.2016).

Figure 12 illustrates the two molecular lines in each disk, scaled in flux and shifted in velocity to focus the comparison on their widths. The H_2 line profiles are stacks of lines in the [1, 4] progression, from Hoadley et al. (in prep). The CO line profiles are stacks of $v = 1$-0 lines from Banzatti & Pontoppidan (2015); Banzatti et al. (2018). The sample is ordered by the infrared index n_{13-31}, which is sensitive to the formation and size of inner disk dust cavities (Banzatti et al. 2020): disks with $n_{13-31} < 0$ are "full" disks (half of this sample), those with $n_{13-31} > 0$ have an inner disk dust cavity

(the other half of the sample). Figure 13 shows the ratio of H_2 to CO full-width-at-half-maximum (FWHM) as a function of n_{13-31}, to analyze a trend that is visible in the line profiles: full disks have similar H_2 and CO line widths, suggesting a similar radial distribution, while disks with a cavity have CO lines narrower than H_2, implying that CO is depleted in an inner disk region where H_2 still survives. The data are significantly correlated, with a Pearson coefficient of 0.62 (p-value of 0.02). Two of the full disks, DR Tau and RU Lup, appear as outliers, with CO lines narrower than H_2 lines; these stars are known to have outflows and might have some low-velocity CO emission from an inner disk wind (Pontoppidan et al. 2011).

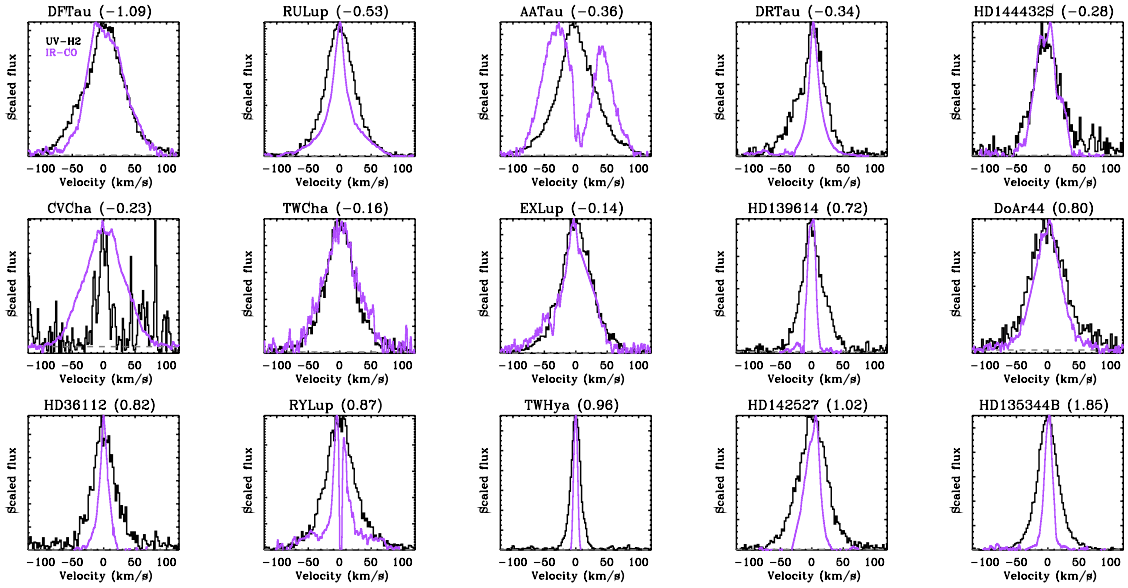

Figure 12. Comparison of CO (purple) and H_2 (black) line profiles for the whole sample ordered by infrared index n_{13-31} (shown next to each target name).

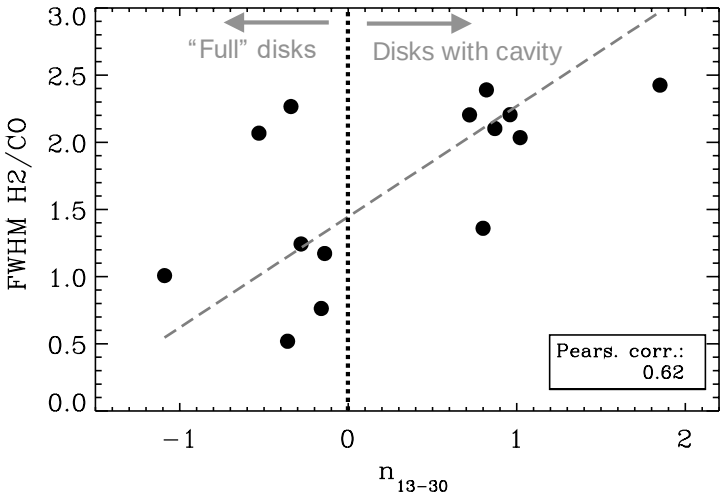

Figure 13. The ratio of H_2 to CO lines FWHM as a function of n_{13-31}. A linear fit is shown with a dashed grey line, highlighting a trend that is already visible in the CO and H_2 line profiles, where CO lines are narrower than H_2 in disks with a cavity.

II.3 Results & Discussion

The empirical difference in H_2 and CO line profiles between full disks and disks with cavities (section II.2) is accompanied by a significant difference in CO excitation. We construct rotation diagrams from the available CO $v = 1\text{-}0$ emission lines observed in each disk. Apart from a vertical shift, which can be given by different emitting areas, the shapes of rotation diagrams match very well in each disk group according to their negative or positive infrared index n_{13-31}. We therefore average them in their respective group and show these averages in figure 14. At upper-level energies $E_{up} > 3500$ K, the two average curves diverge, with cavity disks having a steeper slope than full disks. This difference can be interpreted as colder emission in disks with an inner cavity, although non-LTE excitation can also mimic similar effects (Goldsmith & Langer 1999). While their interpretation is still open, we conclude that strong empirical trends are visible in the data where as disks develop inner dust cavities, CO gas recedes to larger disk radii as

compared to H_2, and CO excitation changes either in temperature or in departure from LTE. Future modeling of these combined spectral datasets promises to reveal key aspects of the physical and chemical evolution of inner disk molecular gas at the time of planet formation.

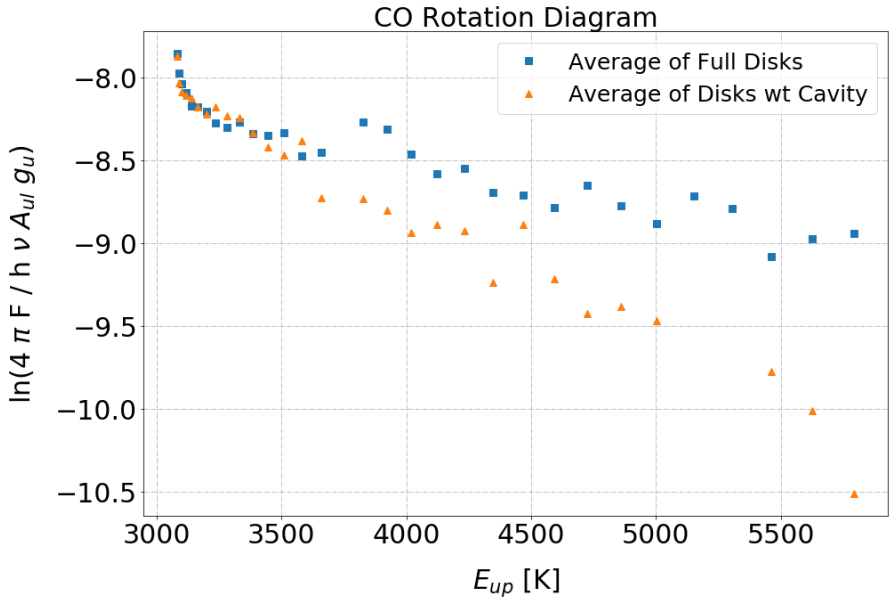

Figure 14. CO rotation diagram for full disks and disks with a cavity.

III. SPECTROSCOPIC DATA ANALYSIS OF SAMPLE

The fundamental emission lines (v = 1-0) of the P-branch in the CO spectrum of 15 disks around T-Tauri and Herbig Ae/Be stars are the focus of the analysis. All spectra were observed using VLT-CRIRES (Kaeufl et al. 2004) except for HD 36112 which was taken with IRTF-iSHELL (Rayner et al.2016). Spectral resolution ($R = \lambda/\Delta\lambda$) for all disks average close to 100,000 for the entire sample with the exception of HD36112 whose spectral resolution is 80,000. The signal-to-noise (S/N) for a given spectrum is ~100. The data, in its present form, is reduced prior to analysis (Banzatti and Pontoppidan 2015 and Banzatti et al. 2018); spectra are not flux-calibrated but are corrected for telluric absorption and continuum-normalized globally. The units of the reduced spectra are in Jansky (Jy) and micron (μm) as seen in figure 15.

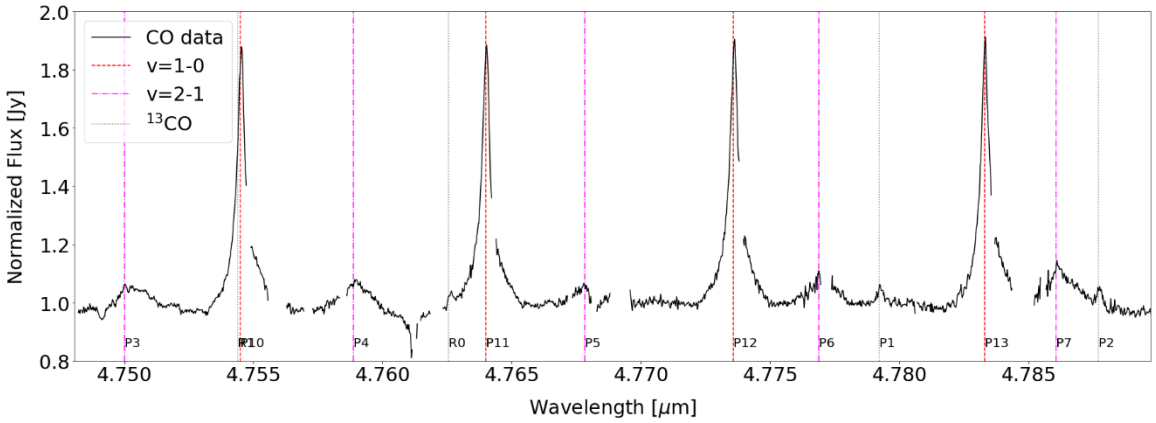

Figure 15. Section of the spectral range coverage of RU Lup. Rovibrational emission lines from ^{13}CO and P- and R-branch lines of ^{12}CO are shown.

Section III.1.1 discusses the emission line identification process in the spectra. Recoverable emission lines are fit with a first-order polynomial continuum in section

III.1.2 which is subtracted from the line. Subsequently, in section III.1.3, the line is best fit with a scaled stacked line profile. Section III.1.4 details the line flux calculation in between this best-fit line profile and the continuum. In section III.2, the rotation diagram technique is used to simultaneously interpret the measured line fluxes from the data and line fluxes extracted from synthetic CO spectrum models. The synthetic spectrum model assumes the CO emission originates from a region in local thermal equilibrium (LTE) at Keplerian rotational velocity around the host star, as described in section III.3. This method is used as a preliminary step to help constrain the excitation temperature and column density that produces the CO spectra observed from inner protoplanetary disks in the primordial stages of disk dispersal.

Analyses, plotting, and computational methods were accomplished in Jupyter Notebook and PyCharm: Python application and an integrated development environment (IDE) written in Python, respectively. The computational tools included were either adopted from previous IDL routines or created originally with new routines in Python.

III.1 Emission Line Flux Measurement

Line flux measurement protocols followed closely the methodology in works by Banzatti and Pontoppidan (2015) and Brown et al. (2013). The measurement of the emission line flux is defined as calculating the area contained between the curve of the transition line and the continuum level. The procedure to measure line fluxes presented in this thesis adopts the techniques from the methods of previous authors: (Salyk et al. 2009; 2011, Banzatti et al. 2011; 2015). Generally, the emission lines suitable for flux

calculation are fitted with a high signal-to-noise (S/N) profile, continuum-subtracted, and integrated to find the true flux, as shown by the gray area in figure 16.

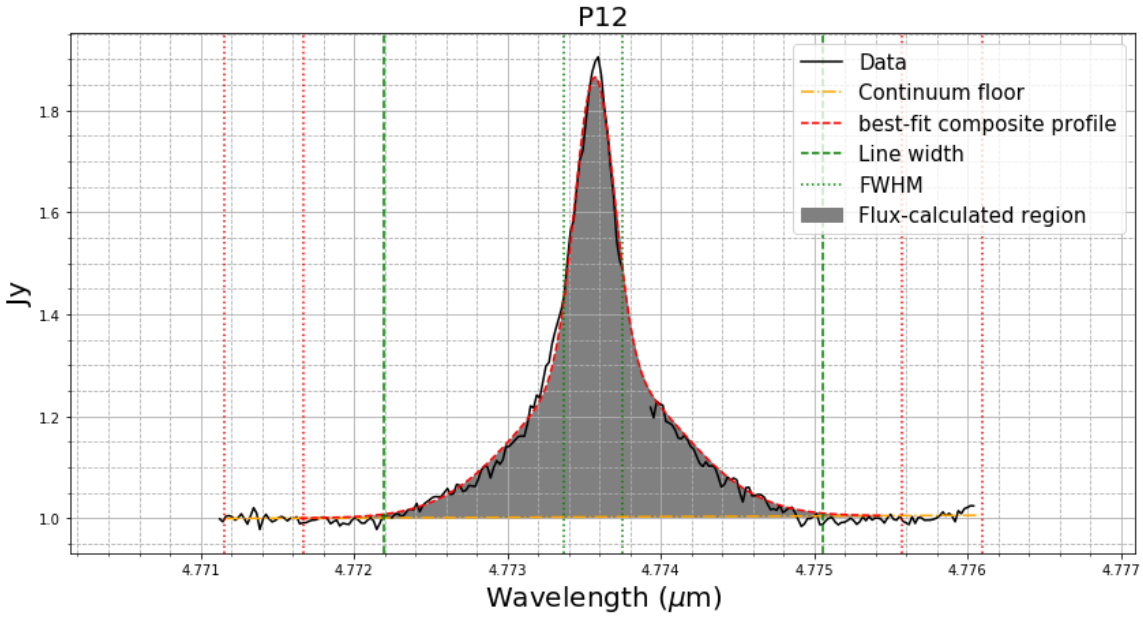

Figure 16. $J = 12$ emission line from the P-branch of rovibrational CO spectra from RU Lup.

III.1.1 *Isolating Emission Line Profiles*

A single spectrum may contain anywhere from 8 (DF Tau and HD 139614) to 38 (HD 36112) fundamental emission lines, consequently a meticulous emission line-finding algorithm was produced to operate recursively through each spectrum for every disk in the sample. However, reduced CO emission spectra are susceptible to telluric correction gaps, contamination from higher vibrational level transitions, detector chip gaps, and noisy continuum (figure 15). Therefore, the code is supervised for each line candidate.

Rovibrational CO emission line center wavelengths obtained from the high-resolution transmission absorption database (HITRAN; https://hitran.org/) identify wavelengths for thermal emission from CO gas at rest. In reality, the spectral emission lines will often be redshifted or blueshifted depending on the radial velocity of the CO

gas in reference to Earth. To aid in the analysis of spectra, the Doppler shift was corrected by subtraction. The at-rest center is then used as a reference point from which to measure the full width at zero intensity (FWZI) – distance between the continuum around the emission line. Line widths are collected and used to differentiate the emission line from the local continuum. For disks with complex features, such as the central absorption in AA Tau and RY Lup, line widths had to be manually identified from the local continuum.

At this stage, the criteria to accept or reject an emission line candidate for analysis depends upon contamination from higher vibrational transitions, missing data (due to telluric correction or detector gaps), and "by-eye" judgment. For example, a well-behaved spectrum is already shown in figure 15, where fundamental emission lines (Δv =1-0) are clearly distinguished from their excited surroundings. While a gap in the emission line is evident around 4.6638 μm, the true shape of the line profile can still be retained (figure 16). These criteria tend to catch most incomplete lines, while the rest are manually judged.

III.1.2 *Continuum Fitting*

The local continuum can be approximated with a 1st order polynomial fit (linear) to differentiate the emission line from the continuum floor. Spectral regions of at least 3 data points on either side of the emission line are selected to establish a fit to the continuum. In practice, each line samples a range of roughly 5×10^{-4} μm (depending on the pixel sampling of the spectrum) on either side of the emission line. For most cases, however, the continuum is detected and fitted from both sides of the emission line. The values of the continuum are fed into the numpy.polyfit() Python routine which

produces a first-order polynomial that best represents the input values. This resulting fit serves as the continuum floor in the analysis.

III.1.3 *Composite Line Profile*

High S/N line profiles were generated by Banzatti and Pontoppidan (2015), wherein a full description of the procedure can be found. Essentially, the stacked line profiles are used in the analysis to increase the S/N of the data and recover previously rejected lines. Each spectrum therefore contributes a single composite, or stacked, line profile.

Emission line profiles are converted from wavelengths to velocities prior to fitting the stacked line profile. The stacked line profiles are fit to emission line peaks by a scaling factor. If the stacked line profile truly represents the shape of all lines in a single spectrum, then the only fitting parameter to fit is the peak value of each line. In other words, the scaling factor is to match the peak of the stacked line profile to the peak of the emission line detected in the data. The χ^2 value is determined from the scaled line profile and the data:

$$\chi^2 = \sum_{i=1}^{n} \frac{(x_i - \mu_i)^2}{\sigma_i^2} \qquad \text{(III.a)}$$

For every i^{th} pixel, x_i is the flux density value of the data, μ_i is the flux density value of the scaled, stacked line profile, and σ_i is the uncertainty in the data. Practically, the stacked line profile must be resampled according to the data available to acquire a χ^2 minimum. The sum is carried out over the entire line width of available data and composite line. Scale factors from 0.0 to 2.75 at a 0.01 interval were tested and subsequently minimized by chi-square to summon the best stacked line fit to the data.

III.1.4 *Integrated Line Flux*

Best-fit line profile composites are then used to calculate emission line flux, otherwise referred to as line intensity (red, dashed curve in figure 16). Ultimately, the line intensity is a sum over all values of flux density present within the line width range. Line intensity is formally calculated:

$$F(erg\ s^{-1}cm^{-2}) = \int F_\nu dv.$$

This expression assumes an infinite pixel sampling, meanwhile the data is limited to a finite pixel sampling. Consequently, the flux calculation is simplified from an integral to a sum over N pixels of flux density (Rybicki & Lightman 2004):

$$F(erg\ s^{-1}cm^{-2}) = \sum_{i}^{N} px_i \cdot f_i. \qquad \text{(III.b)}$$

The factors in the sum correspond to the pixel width in wavelength units (μm) and the value of flux density, respectively. Values for px_i are set by the instrument detector and resolution. In terms of units, the data are converted from micron and Jansky to provide fluxes in erg s^{-1} cm^{-2} Hz.

As an added check, the measured line fluxes were plotted versus their respective J-level to identify potential outliers. This step serves to quickly check the goodness-of-fit and to identify potential outliers in the line flux measurements, which were then inspected for problems (e.g., an incorrect continuum fit, or blending with other lines).

The calculation of error propagation followed methods described in Taylor's *Introduction to Error Analysis 2nd ed.* Considering equation (III.b), the calculation of flux density uncertainty is therefore

$$\delta f = \sqrt{(\delta f_1)^2 + (\delta f_2)^2 + (\delta x_3)^2 + \cdots}, \tag{III.c}$$

where f_1, f_2, f_3, … represent the flux density value for the first, second, and third pixel, respectively. Consequently, δf_n (for $n = 1, 2, 3$ ...) is the uncertainty in flux density for the corresponding nth pixel. To calculate the rest of the uncertainty in flux density, the uncertainty in the continuum fit must be determined. Local line continua are approximated with a linear regression curve and its propagation of error:

$$y = mx + b,$$

$$\therefore \delta y_i = \sqrt{(px_i \cdot \delta m_i)^2 + (\delta b_i)^2}. \tag{III.d}$$

The quantity px_i is the same as in equation (III.b). Values for m_i and b_i are found from the linear continuum fit from Section (III.1.2). This uncertainty is added to the flux density uncertainty to retrieve the net error accumulated in the emission line:

$$\delta f_{net} = \delta f_i + \delta y_i$$

Thus, the expression to calculate the error for the flux calculation is

$$\delta F = \sqrt{\sum_i^N (px \cdot \delta f_{net})^2} = px \sqrt{\sum_i^N (\delta f_{net})^2}$$

Because $\delta f_{net} = \delta f_i + \delta cont$, where $\delta cont$ is represented as δy_i in equation (III.d), the total flux error is whittled into

$$\therefore \delta F = px \sqrt{\sum_i^N \left(\delta f_i + \sqrt{(px_i \cdot \delta m_i)^2 + (\delta b_i)^2}\right)^2}, \tag{III.e}$$

where N is the total number of pixels within an emission line and the local continuum.

III.2 Rotation Diagram

III.2.1 *Application to this Sample*

Rotation diagrams for the sample were created using line intensities and frequencies measured from the data. Einstein A-coefficients and statistical weights corresponding to the upper- to lower-level transitions were taken from HITRAN database. Upper-level energies are similarly acquired for the appropriate frequencies. Recalling equation (I.a) in Section I.2.4, the y-axis is a function of the measured line flux. The x-axis consists of the energy from the upper state of the transition identified by its frequency divided by the Boltzmann constant as seen in equation (I.b). X versus Y plots for the measured spectra are then generated and shown in figures 17 and 18.

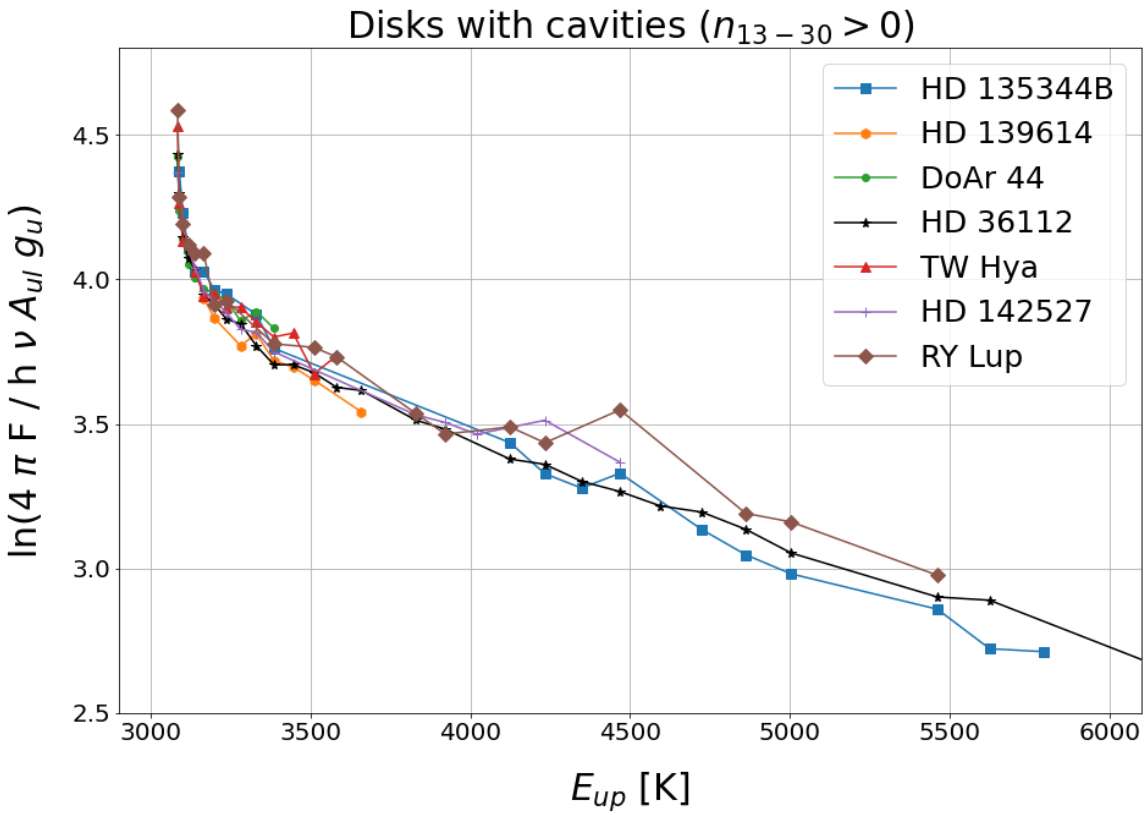

Figure 17. Rotation diagram of all disks with a cavity in the sample as indicated by their infrared index. Each disk was normalized at low wavelengths to compare their curvatures.

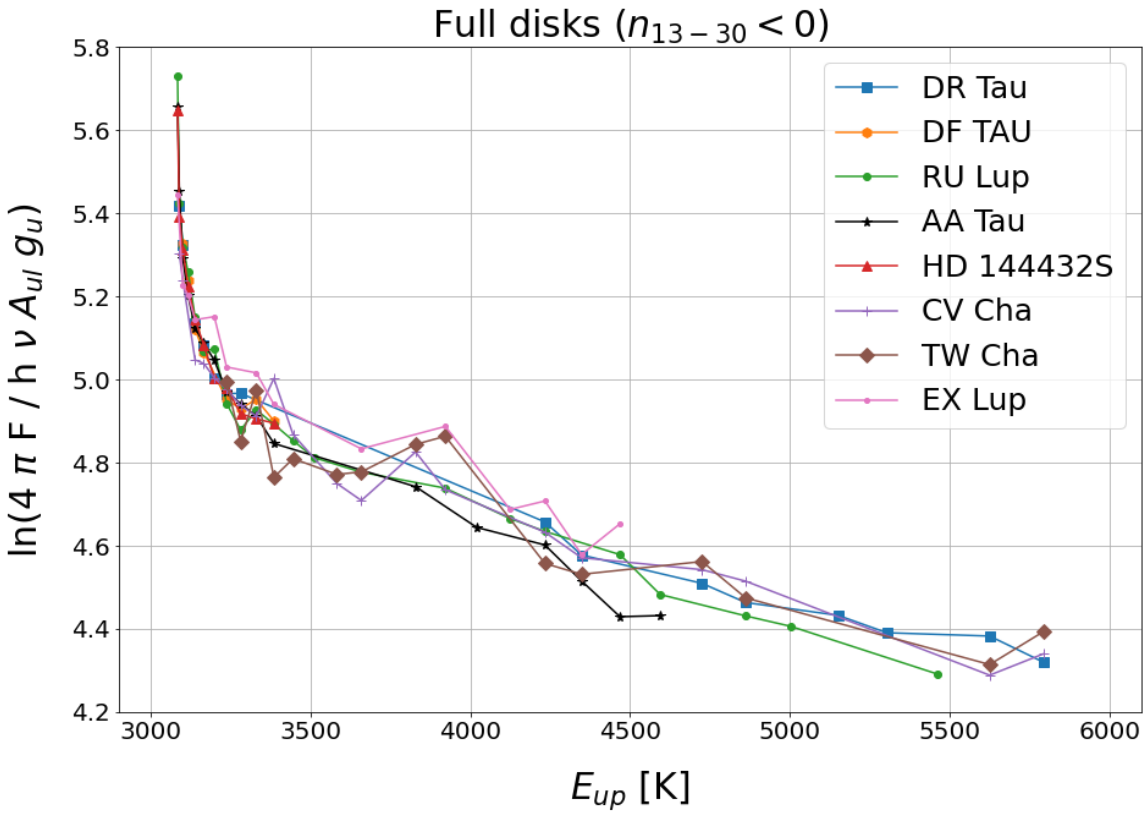

Figure 18. Rotation diagram of all full disks in the sample as indicated by their infrared index. Similar to figure 17, each disk spectra were normalized accordingly.

III.3 Local Thermal Equilibrium Single Slab Model

The model itself exists as a Python package whose functions are used to generate the spectra from a single slab of thermalized CO gas with optical thickness N_{CO}, excitation temperature T_{ex}, and emitting area as a function of radius, $A(R) = 2\pi R^2$ (note the model actually produces an emitting solid angle, Ω, but the distance to the target is known, thus resulting in an emitting area). The calculations used in generating the theoretical spectrum are detailed in the Appendix from Banzatti et al. 2012. The keys to using such a model are the assumptions: the CO excitation levels are thermalized, the emitting region is in LTE, and emission lines have a Gaussian profile.

III.3.1 *Model Parameters*

The CO spectra is fitted with a simple LTE model. The model assumes CO emission is generated by a gas ring in LTE that is rotating about the host star at Keplerian velocity (Salyk et al. 2007a, Banzatti et al. 2012). In order to produce such a spectrum, the model requires several parameters: (1) wavelength minimum and maximum for the entire spectrum, (2) pixel sampling, (3) line width (broadening due to excitation), (4) distance, (5) intrinsic line width, (6) excitation temperature, (7) column density, and (8) radius of emitting area. Table 3 includes information about the parameters and ranges of values.

Table 3. LTE model input parameters.

Index	**Symbol**	**Unit**	**Description: Range of values**
(1)	λ_{min}, λ_{max}	μm	Spectral range over which to create CO spectra: $4.2\ \mu\text{m} - 5.3\ \mu\text{m}$
(2)	dλ	μm/px	Wavelength coverage per pixel: $2 \times 10^{-4}\ \mu$m/px
(3)	FWHM	km/s	Line width: ~7.5 km/s < FWHM < ~60 km/s
(4)	d	pc	Distance to the source: 140 pc
(5)	dν	μm	Intrinsic line width: 1.0 km/s
(6)	T_{ex}	K	Excitation temperature: 10^2 K < T_{ex} < 10^3 K
(7)	N_{CO}	cm^{-2}	Column density: 10^{15} cm^{-2} < N_{CO} < 10^{21} cm^{-2}
(8)	R_{norm}	AU	Radius of emitting area: 0.2 AU < r < 1.5 AU

The spectral resolution is given by the FWHM of the emission line velocity profiles. With the constants (1) – (5) pertaining to the CO molecule and emission, instrument resolution, and physical distance, the three parameters (6) – (8) are the focus

of this work: T_{ex}, N_{mol}, R_{norm}.

III.3.2 *Modeling Procedure and Output*

Firstly, the model is fed values for the integrated line fluxes (as measured in section III.1), their uncertainty, and their line widths. These data are best reproduced by the molecular emission model as identified by the chi-square test. The accumulated chi-square values for each line in the spectrum compose the chi-square total for the model and data. In order to find the absolute best fit compared to the matched spectra of other disks, the reduced chi-square ($\tilde{\chi}^2$) is used. The reduced chi-square factor is found simply by dividing the result of (III.a) by the number of degrees of freedom:

$$\tilde{\chi}^2 = \frac{\chi^2}{d}.$$

The number of degrees of freedom is defined as the difference between the number of data points (number of line flux measurements per spectrum) and free parameters (excitation temperature + column density + emitting radius = 3). According to the reduced chi-square test, the goodness-of-fit increases as the reduced chi-square ratio approaches unity.

To mitigate the degeneracy in χ^2, a 3-D grid of LTE slab models create the parameter space from which to minimize χ^2. Each dimension of the grid is occupied by the rotational temperature, column density, and radius. Start/stop ranges for the three parameters are shown in table 3. There are 10 values between the stop/start ranges for all three parameters which are equally spaced out on a log scale. This creates a 3-D grid of values which are mixed and combined to form a coarse grid of LTE models, each with a corresponding chi-square. χ^2 plots of the temperature and column density from the model are then generated to better identify where degeneracies exist.

Once verified by-eye, the three coarsely minimized parameters are then carried over to the finer, simplex algorithm (Nelder and Mead 1965) which will find the absolute grid minimum starting from the coarse grid minimized parameters. The double minimization method reduces the probability of degenerate χ^2 minima. This effectively concludes the fitting procedure and outputs a synthetic, rovibrational CO spectrum corresponding to the final rotational temperature, column density, and emitting radius determined from the double minimization.

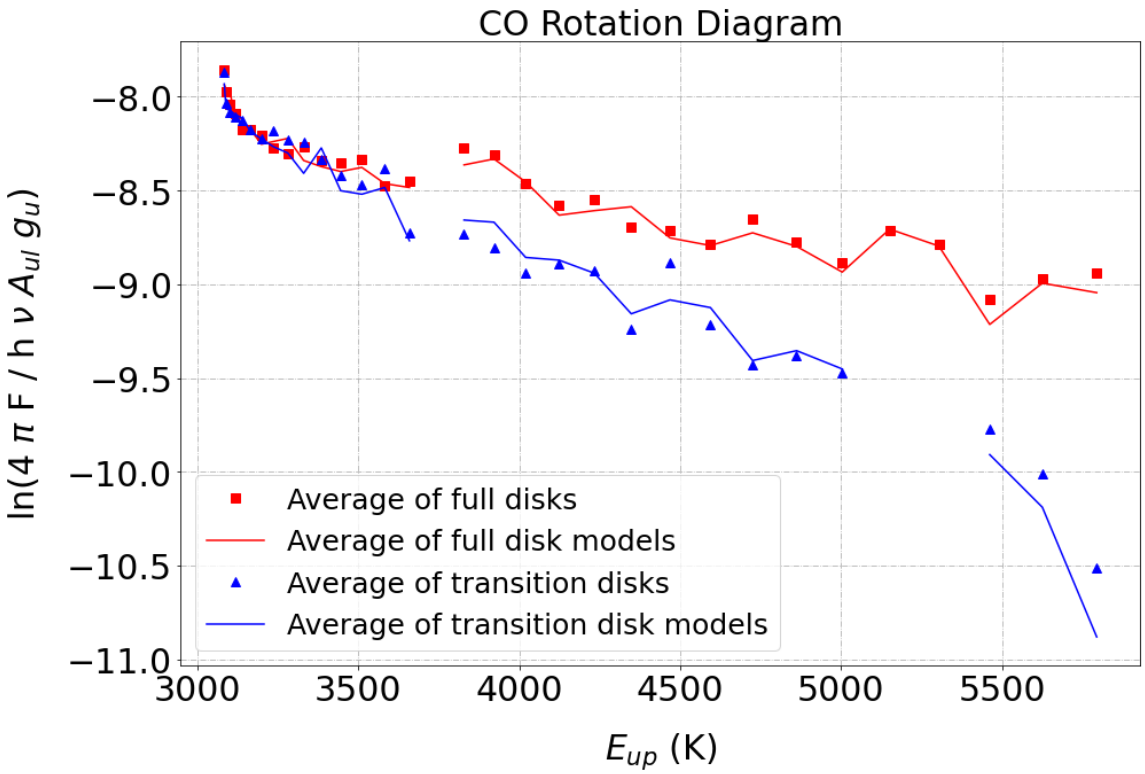

Figure 19. Rotation diagram of full and transitional disk line flux averages plotted with model flux averages.

IV. CONCLUSION

IV.1 Results

Table 4. Sample properties with derived LTE model results.

Star Name	M_*	L_*	$\log L_{acc}$	n_{13-31}	Dust cavity (AU)	T_{rot} (K)	$\log N$ (cm^2)
DF Tau	0.6	0.6	-0.63	-1.09	-	1283	17.3
RU Lup	0.55	1.45	-0.01	-0.53	-	1160	17.3
AA Tau	0.6	0.5	-1.43	-0.36	28	765	17.4
DR Tau	0.93	0.63	-0.24	-0.34	-	987	17.5
HD 144432S	1.7	14.8	-0.35	-0.28	-	431	17.4
CV Cha	2.1	8	-0.41	-0.23	-	1129	16.9
TW Cha	1.0	0.38	-1.66	-0.16	-	585	18.7
EX Lup	0.5	1.1	-1.3	-0.14	-	1226	16.8
HD 139614	1.5	6.6	-0.1	0.72	6	587	16.0
Do Ar 44	1.22	0.93	-0.73	0.8	34	850	16.7
HD 36112	1.56	11	-0.1	0.82	62	671	17.3
RY Lup	1.127	1.82	-1.4	0.87	68	342	18.7
TW Hya	0.61	0.23	-1.53	0.96	2.4	559	17.2
HD 142527	2	16.3	0.8	1.02	120	706	17.3
HD 135344B	1.43	6.17	-1.11	1.85	62	551	17.2

Fitted model results are reported in table 4. The fundamental rovibrational emission is fitted by the LTE model to reproduce excitation observed in CO spectra. For the 15 full and transition disks in the sample, 71% of full disks correspond to high excitation temperatures ($T_{ex} \gtrsim 1000$ K); ~88% of disks with a central dust cavity indicate excitation temperatures that are expectedly colder ($T_{ex} < 900$ K). These temperatures largely coincide with the presence/absence of a dust cavity. Excluding AA Tau, almost all full disks with a negative infrared index value are paired with higher CO excitation temperatures compared to transition disks which correlate lower temperatures and positive infrared indices (figure 19).

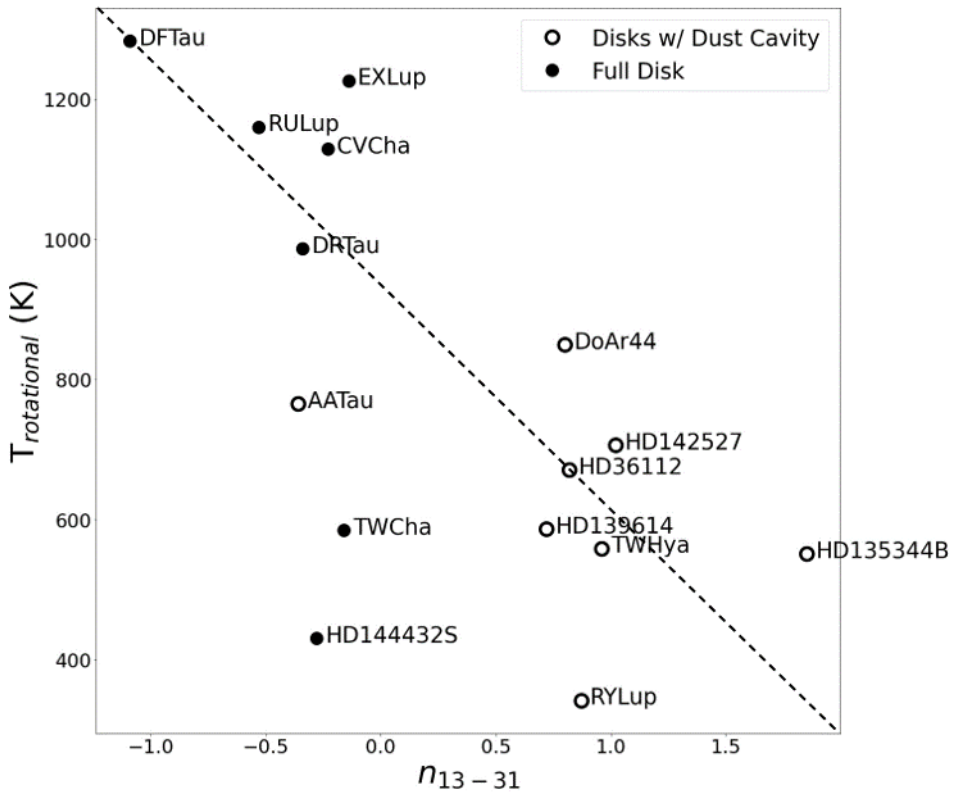

Figure 20. Comparison plot for rotational temperature and spectral index. The dashed black line is the function $y = -x$. The vertical axis is the excitation temperature derived from the LTE model. The x-axis represents dust presence close to the star.

Beyond $E_{up} = 3500$ K, the rotation diagram averages for both types of disks diverges (figure 19) which results in a difference in excitation temperature. From the rotation diagram, higher average CO temperatures are derived in full disks while colder excitation temperatures are found in disks with a cavity (section I.2.4). At high upper-level energies, the LTE model fails to predict accurate excitation intensities as apparent in the lower average model flux curve. CO FWHM narrow with the depletion of inner disk dust compared to H_2 FWHM which remains broader by comparison for positive values of infrared index: a trend reflected in figure 13.

IV.2 Discussion

The distribution of excitation temperatures relative to full disks and disks with cavities insinuates a correlation between colder CO gas temperatures and larger radii (figure 20). This result is further reinforced by larger H_2 FWHM (full width at half-maxima) compared to CO FWHM which serves as a tentative indicator for H_2 presence at smaller radii where CO recedes (figure 21). Salyk et al. (2011) also found systematically lower rotational temperatures for transitional disks correlating to the ratio of CO inner radius to the dust sublimation radius. Furthermore, in their study the authors also found a deviation in temperature between black-body grains and CO gas located at the inner CO radius suggesting a decoupling from predicted dust temperature (Najita et al. 2003, Brittain et al. 2009). A similar analysis and result were modeled by Chiang and Goldreich in 1997 – gas atmosphere temperatures exceeded those of the dust emission by 3 orders of magnitude.

As mentioned in section I.1.1, the infrared index is susceptible to change as a function of viewing geometry. This creates discrepancies for highly inclined disks such as AA Tau, DF Tau, TW Cha, (Banzatti et al. 2017; 2020). However, n_{13-31} still effectively measures gas content at small radii of PPDs. Figure 20 empirically presents the picture of dissipating inner disks as a function of dust emission cavities by correlating linewidth to inner disk cavity presence. Figure 21 demonstrates the radial stratification of molecular gas through decreasing emission line widths with decreasing excitation temperatures.

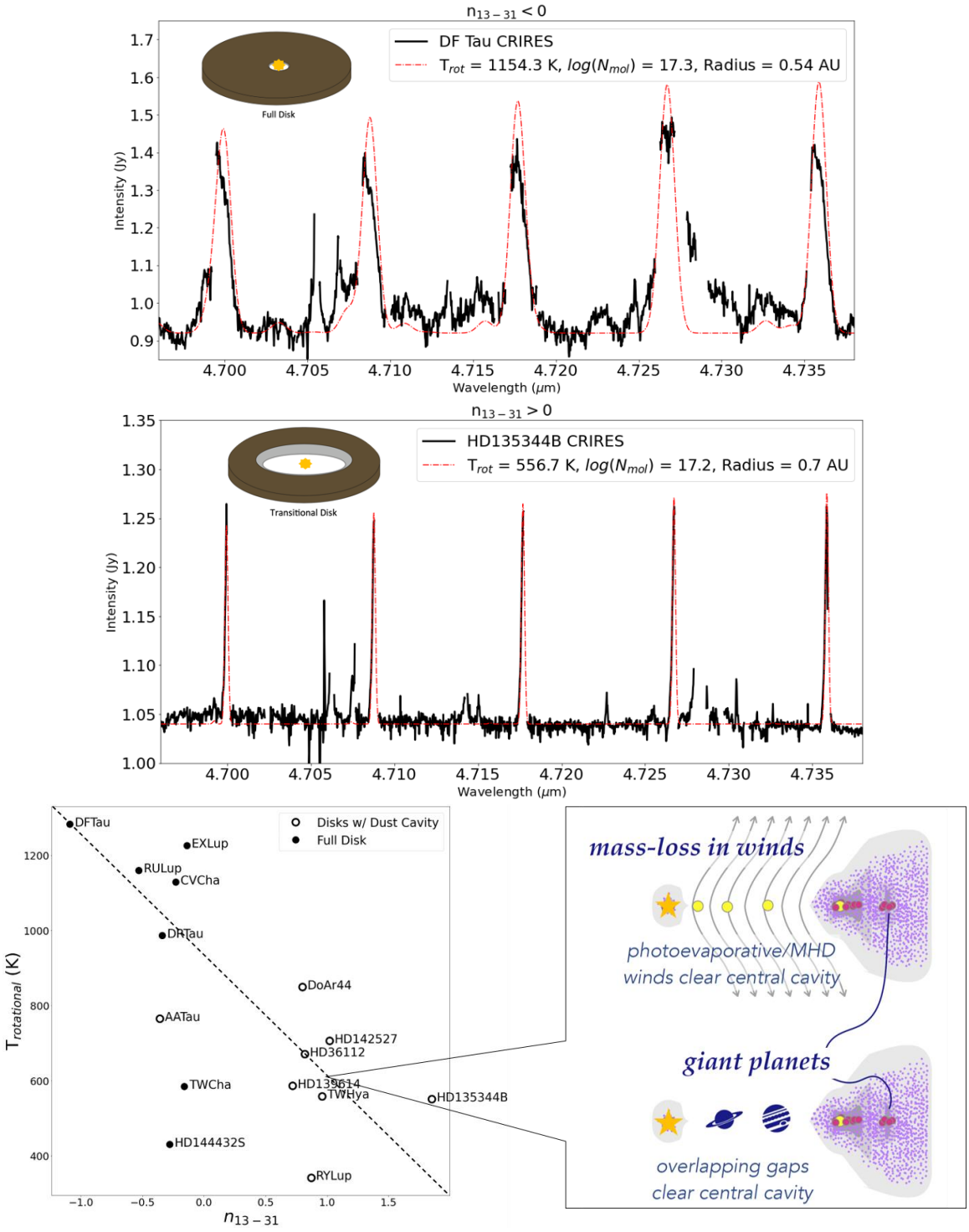

Figure 21. Comparison between spectra and derived rotational temperatures of full and transition disks. *Top & Middle Panels:* CO $\Delta v = 1$ emission lines fitted with LTE excitation model (red, dashed line). *Bottom Right:* Cartoon of potential gap-clearing mechanisms. *Bottom Left:* The same plot is depicted in figure 19.

At larger wavelengths, the LTE model underestimates measured line fluxes. This can be due to a variety of likely physical mechanisms including non-LTE excitation (Salyk et al. 2009, Herczeg et al 2011), radial temperature and/or column density gradients, as well as dynamic factors like molecular outflows, winds, and jets (Ercolano and Pascucci 2017). From figure 19 it is evident that there is a significant deviation in upper-level energies ($E_{up} > 3500$ K) for full disks and disks with a cavity (transition disks). The divergence in excitation suggests a higher overall temperature for CO gas close to the star in full disks due to the gradual curvature at higher upper-level energies. Granted, LTE fits alone cannot reproduce the rovibrational CO emission observed, it sets a lower bound for the CO gas temperature in inner gaseous disks (Salyk et al. 2009).

IV.3 Future Work

To further exhaust the information held within rich spectra, a more sophisticated treatment would be needed to explicitly interpret the excitation spectra. An approach to distinguish distinct excitation sources is to separate each emission line by its components: broad component (BC) and narrow component (NC). The BC traces faster-moving gas while the NC denotes the emission of slower-moving gas at larger radii – assuming Keplerian motion. The broad wings of full disk emission lines are not well fit with the simple LTE model, as the model and data diverge for larger wavelengths. Therefore, fitting both the $v = 1$-0 and $v = 2$-1 transitions separately will offer the first step towards decomposing the spectra. Isolating excitation sources for each vibrational level will assist in determining what mechanisms cause certain line profiles to arise and how to categorize them into an evolutionary track.

As a proxy for the BC (hotter CO) and NC (colder CO), a single LTE model can be used to fit the temperature and column density profiles for higher excitation vibrational levels, $v = 2\text{-}1$, to mimic the contribution due to hot CO (BC). This contribution is thusly subtracted from the data to yield residuals that ideally isolate the excitation contribution. A new LTE model is then fit to the residual $v = 1\text{-}0$ emission. Two temperatures will then characterize the region in the PPD: a column density and an excitation temperature for $v = 2\text{-}1$ emission and $v = 1\text{-}0$ residual emission. This approach adds a level of rigor to the LTE fitting procedure and achieves better fits for higher upper-level energies.

REFERENCES

ALMA Partnership et al. 2015. "The 2014 ALMA Long Baseline Campaign: First Results from High Angular Resolution Observations Toward the HL Tau Region." *The Astrophysical Journal Letters* 808, no. 1 (July): L3-L13.

Alexander R., I. Pascucci, S. Andrews, P. Armitage, L. Cieza. 2014. "The Dispersal of Protoplanetary Disks." In *Protostars and Planets VI*, edited by Henrik Beuther, Ralf S. Klessen, Cornelis P. Dullemond, Thomas Henning, 475-496. Tuscon, Arizona: University of Arizona Press. https://doi.org/10.2458/azu_uapress_9780816531240-ch021.

Allen, T. S. et al. 2017. "Properties of the Closest Young Binaries. I. DF Tau's Unequal Circumstellar Disk Evolution." *The Astrophysical Journal* 845, no. 2 (August): 161. https://doi.org/10.3847/1538-4357/aa8094.

Andrews, Sean M. et al. 2014. "Resolved Multifrequency Radio Observations of GG Tau." *The Astrophysical Journal* 787, no. 2 (June): 148. https://doi.org/10.1088/0004-637X/787/2/148.

Andrews, Sean. 2020. "Observations of Protoplanetary Disk Structures." *Annual Review of Astronomy and Astrophysics* 58 (August): 1-49. https://doi.org/10.1146/annurev-astro-031220-010302.

Andrews, Sean M. et al. 2016. "Ringed Substructure and a Gap at 1 au in the Nearest Protoplanetary Disk." *The Astrophysical Journal Letters* 820, no. 2 (April): L40. https://doi.org/10.3847/2041-8205/820/2/L40.

Armitage, Philip J., and Wilhelm Kley. 2019. *From Protoplanetary Disks to Planet Formation*. Edited by Marc Audard, Michael R. Meyer, Alibert Yann. Germany: Springer.

Armitage, Philip J. 2020. *Astrophysics of Planet Formation.* 2nd ed. New York: Cambridge University Press.

Arulanantham, N. et al. 2018. "A UV-to-NIR Study of Molecular Gas in the Dust Cavity around RY Lupi." *The Astrophysical Journal* 855, no. 2 (March): 98. https://doi.org/10.3847/1538-4357/aaaf65.

Bast J. E., J. M. Brown, G. J. Herczeg, E. F. van Dishoeck, K. M. Pontoppidan. 2011. "Single peaked CO emission line profiles from the iner regions of protoplanetary disks." *Astronomy and Astrophysics* 527, (March): A119. https://doi.org/10.1051/0004-6361/201015225.

Banzatti, A., M. R. Meyer, S. Bruderer, V. Geers, I. Pascucci, F. Lahuis, A. Juhász, T. Henning, P. Ábrahám. 2012. "EX Lupi from Quiescence to Outburst: Exploring the LTE Approach in Modelling Blended H_20 and OH Mid-Infrared Emission." *The Astrophysical Journal* 751, no.1 (January): 90. https://doi.org/10.1088/0004-637X/745/1/90.

Banzatti, A., K. M. Pontoppidan, S. Bruderer, J. Muzerolle, and M. R. Meyer. 2015a. "Depletion of Molecular Gas by an Accretion Outburst in a Protoplanetary Disk." *The Astrophysical Journal Letters* 798, no.1 (January): L16-L22. https://doi.org/10.1088/2041-8205/798/1/L16.

Banzatti, A., P. Pinilla, L. Ricci, K. M. Pontoppidan, T. Birnstiel, and F. Ciesla. 2015b. "Direct Imaging of the Water Snow Line at the Time of Planet Formation Using Two Alma Continuum Bands." *The Astrophysical Journal Letters* 815, no. 1 (December): L15-L21. https://doi.org/10.1088/2041-8205/815/1/L15.

Banzatti, A. and K. M. Pontoppidan. 2015. "An Empirical Sequence of Disk Gap Opening Revealed by Rovibrational CO." *The Astrophysical Journal* 809, no. 2 (August): 167. https://doi.org/10.1088/0004-637X/809/2/167.

Banzatti, A. K. M. Pontoppidan, C. Salyk, G. J. Herczeg, E. F. van Dishoeck, E. F. Blake. 2017. "The Depletion of Water During Dispersal of Planet-forming Disk Regions." *The Astrophysical Journal* 834, no. 2 (January): 152. https://doi.org/10.3847/1538-4357/834/2/152.

Banzatti, A. A. Garufi, M. Kama, M. Benisty, S. Brittain, K. M. Pontoppidan, J. Rayner. 2018. "Observing the Linked Depletion of Dust and CO Gas at 0.1-10 au in the Disks of Intermediate-Mass Stars." *Astronomy and Astrophysics* 609, (March): L2.

Banzatti, A., I. Pascucci, A. Bosman, P. Pinilla, C. Salyk, G. Herczeg, K. Pontoppidan et al. 2020. "Hints for icy pebble migration feeding an oxygen-rich chemistry in the inner planet-forming region of disks." *The Astrophysical Journal* 903, no.2 (November): 124. https://doi.org/10.3847/1538-4357/abbc1a.

Banzatti, A., I. Pascucci, S. Edwards, M. Fang, U. Gorti, M. Flock. 2019. "Kinematic Links and the Coevolution of MHD Winds, Jets, and Inner Disks from a High-resolution Optical [O I] Survey." *The Astrophysical Journals* 870, no. 2 (January): 76. https://doi.org/10.3847/1538-4357/aaf1aa.

Banzatti, A. et al. 2020. "Hints for Icy Pebble Migration Feeding an Oxygen-rich Chemistry in the Inner Planet-forming Region of Disks." *The Astrophysical Journal* 903, no. 2 (November): 124. https://doi.org/10.3847/1538-4357/abbc1a.

Bergin, E. A. et al. 2010. "Sensitive Limits on the Abundance of Cold Water Vapor in the DM Tauri Protoplanetary Disk." *Astronomy and Astrophysics* 521, (June): L33. https://doi.org/10.1051/0004-6361/201015104.

Bitner, Martin A. et al. 2008. "The TEXES Survey for H_2 Emission from Protoplanetary Disks." *The Astrophysical Journal* 688, no. 2 (December): 1326-1344. https://doi.org/10.1086/592317.

Boley, Aaron C. 2009. "The Two Modes of Gas Giant Planet Formation." *The Astrophysical Journal Letters* 695, no.1 (March): L53-L57. https://doi.org/10.1088/0004-637X/695/1/L53.

Boss, Alan P. and Harold W. York. 1996. "Protoplanetary Disks, Mid-Infrared Dips, and Disk Gaps." *The Astrophysical Journal* 469, (September): 366. https://doi.org/10.1086/177786.

Brittain, Sean, T. Simon, J. Najita, T. Rettig. 2007. "Warm Gas in the Inner Disks around Young Intermediate-Mass Stars." *The Astrophysical Journal* 659, no. 1 (April): 685-704. https://doi.org/10.1086/511255.

Brittain, Sean D., Joan R. Najita, and John S. Carr. 2009. "Tracing the Inner Edge of the Disk Around HD 100546 with Rovibrational CO Emission Lines." *The Astrophysical Journal* 702, no. 1 (September): 85-99. https://doi.org/10/1088/0004-637X/702/1/85.

Brown, J. M. et al. 2007. "Cold Disks: Spitzer Spectroscopy of Disks around Young Stars with Large Gaps." *The Astrophysical Journal Letters* 664, no. 2 (August): L107-L110. https://doi.org/10.1086/520808.

Brown, J. M., K. M. Pontoppidan, E. F. van Dishoeck, G. J. Herczeg, G. A. Blake, A. Smette. 2013. "VLT-CRIRES Survey of Rovibrational CO Emission from Protoplanetary Disks." *The Astrophysical Journal* 770, no. 2 (June): 94. https://doi.org/10.1088/0004-637X/770/2/94.

Carmona, A. 2009. "Observational Diagnostics of Gas in Protoplanetary Disks." *Earth Moon Planets* 106 (December): 71-95. https://doi.org/10.1007/s11038-009-9347-2.

Chapillon, E. et al. 2012. "Chemistry in Disks. VII. First Detection of HC_3N in Protoplanetary Disks." *The Astrophysical Journal* 756 no. 1 (September): 58. https://doi.org/10.1088/0004-637X/756/1/58.

Chiang, E. I. and P. Goldreich. 1997. "Spectral Energy Distributions of T Tauri Stars with Passive Circumstellar Disks." *The Astrophysical Journal* 490, no. 1 (November): 368-376. https://doi.org/10.1086/304869.

Dutrey A., S. Guilloteau, M. Guelin. 1997. "Chemistry of Protostar-like Nebula: The Molecular Content of the DM Tau and GG Tau Disks." *Astronomy and Astrophysics* 317 (January): L55-L58. https://ui.adsabs.harvard.edu/abs/1997A&A...317L..55D.

Dutrey et al. 2014 "Physical and Chemical Structure of Planet-Forming Disks Probed by Millimeter Observations and Modeling." In *Protostars and Planets VI*, edited by Henrik Beuther, Ralf S. Klessen, Cornelis P. Dullemond, Thomas Henning, 317-338. Tuscon, Arizona: University of Arizona Press. https://doi.org/10.2458/azu_uapress_9780816531240-ch014.

Ercolano B. and I. Pascucci. 2017. "The Dispersal of Planet-Forming Discs: Theory Confronts Observations." *Royal Society Open Science* 4, no. 4 (April). https://doi.org/10.1098/rsos.170114.

Espaillat, C. et al. 2014. "An Observational Perspective of Transitional Disks." In *Protostars and Planets VI*, edited by Henrik Beuther, Ralf S. Klessen, Cornelis P. Dullemond, Thomas Henning, 497-520. Tuscon, Arizona: University of Arizona Press. https://doi.org/10.2458/azu_uapress_9780816531240-ch022.

Fairlamb, J. R., R. D. Oudmaijer, I. Mendigutía, J. D. Ilee, M. E. van den Ancker. 2015. "A Spectroscopic Survey of Herbig Ae/Be Stars with X-shooter – I. Stellar Parameters and Accretion Rates." *Monthly Notices of the Royal Astronomical Society* 453, no. 1 (October): 976-1001. https://doi.org/10.1093/mnras/stv1576.

Fang, M. et al. 2018. "A New Look at T Tauri Star Forbidden Lines: MHD-driven Winds from the Inner Disk." *The Astrophysical Journal* 868 no. 1 (November): 28. https://doi.org/10.3847/1538-4357/aae7.

France, K., G. J. Herczeg, M. McJunkin, S. V. Penton. 2014. "CO/H_2 Abundance Ratio ~10^{-4} in a Protoplanetary Disk." *The Astrophysical Journal* 794, no. 2 (October): 160. https://doi.org/10.1088/0004-637X/794/2/160.

Francis, L. and N. van der Marel. 2020. "Dust Depleted Inner Disks in a Large Sample of Transition Disks Through Long-Baseline ALMA Observations." *The Astrophysical Journal* 892, no. 2 (April): 111-134. https://doi.org/10.3847/1538-4357/ab7b63.

Furlan, E. et al. 2006. "A Survey and Analysis of Spitzer Infrared Spectrograph Spectra of T Tauri Stars in Taurus." *The Astrophysical Journal Supplement Series* 165 no. 2 (August): 568-605. https://doi.org/10.1086/505468.

Furlan, E. et al. 2009. "Disk Evolution in the Three Nearby Star-forming Regions of Taurus, Chamaeleon, and Ophiuchus." *The Astrophysical Journal* 703, no. 2 (October): 1964-1983. https://doi.org/10.1088/0004-637X/703/2/1964.

Herczeg, G. J., J. M. Brown, E. F. van Dishoeck, and K. M. Pontoppidan. 2011. "Disks and outflows in CO rovibrational emission from embedded, low-mass young stellar objects." *Astronomy & Astrophysics* 533, A112 (September): 90-106. https://doi.org/10.1051/0004-6361/201016246.

Hoadley, K., K. France, R. D. Alexander, M. McJunkin, P. C. Schneider. 2015. "The Evolution of Inner Disk Gas in Transition Disks." *The Astrophysical Journal* 812, no. 1 (October): 41. https://doi.org/10.1088/0004-637X/812/1/41.

Gangi, M. et al. 2020. "GIARPS High-resolution Observations of T Tauri stars (GHOsT). II. Connecting Atomic and Molecular Winds in Protoplanetary Disks." *Astronomy and Astrophysics* 643, A32 (November): 20. https://doi.org/10.1051/0004-6361/202038534.

Goldsmith, Paul F. and William D. Langer. 1999. "Population Diagram Analysis of Molecular Line Emission." *The Astrophysical Journal* 517, no. 1 (May): 209-225. https://doi.org/10.1086/307195.

Gorti, U., D. Hollenbach, C. P. Dullemond. 2015. "The Impact of Dust Evolution and Photoevaporation on Disk Dispersal." *The Astrophysical Journal* 804, no. 1 (May): 29. https://doi.org/10.1088/0004-637X/804/1/29.

Lada, C. J. and B. A. Wilking. 1984. "The Nature of the Embedded Population in the Rho Ophiuchi Dark Cloud: Mid-Infrared Observations." *The Astrophysical Journal* 287 (December): 610-621. https://doi.org/10.1086/162719.

Li Z.-Y., B. R. Banerjee, R. E. Pudritz, J. K. Jørgensen, H. Shang, R. Krasnopolsky, A. Maury. "The Earliest Stages of Star and Planet Formation: Core Collapse, and the Formation of Disks and Outflows." In *Protostars and Planets VI*, edited by Henrik Beuther, Ralf S. Klessen, Cornelis P. Dullemond, Thomas Henning, 173-194. Tuscon, Arizona: University of Arizona Press. https://doi.org/10.2458/azu_uapress_9780816531240-ch008.

Long, F. et al. 2019. "Compact Disks in a High-resolution ALMA Survey of Dust Structures in the Taurus Molecular Cloud." *The Astrophysical Journal* 882, no. 1 (September): 49. https://doi.org/10.3847/1538-4357/ab2d2d.

Kaeufl, Hans U. et al. 2004. "CRIRES: a High-resolution Infrared Spectrograph for ESO's VLT." *Ground-based Instrumentation for Astronomy* 5492, (September): 1218-1227. https://doi.org/10.1117/12.551480.

Kastner, J. H., B. Zuckerman, D. A. Weintraub, T. Forveille. 1997. "X-ray and Molecular Emission from the Nearest Region of Recent Star Formation." *Science* 277, (July): 67-71. https://doi.org/10.1126/science.277.5322.67.

Maaskant, K. M., M. Min, L. B. F. M. Waters, A. G. G. M. Tielens. 2014. "Polycyclic Aromatic Hydrocarbon Ionization as a Tracer of Gas Flows through Protoplanetary Disk Gaps." *Astronomy and Astrophysics* 563 (March): A78. https://doi.org/10.1051/0004-6361/201323137.

Manara, C. F. et al. 2016. "Evidence for a Correlation Between Mass Accretion Rates onto Young Stars and the Mass of their Protoplanetary Disks." *Astronomy and Astrophysics* 591 (June): L3. https://doi.org/10.1051/0004-6361/201628549.

Mednigutía, I., J. Fairlamb, B. Montesinos, R. D. Oudmaijer, J. R. Najita, S. D. Brittain, M. E. van der Ancker. 2014. "Stellar Parameters and Accretion Rateo f the Transition Disk Star HD 142527 from X-Shooter." *The Astrophysical Journal* 790, no. 1 (July): 21. https://doi.org/10.1088/0004-637X/790/1/21.

Menu, J., R. van Boekel, T. Henning, C. Leinert, C. Waelkens, L. B. F. M. Waters. 2015. "The Structure of Disks around Intermediate-Mass Young Stars from Mid-Infrared Interferometry. Evidence for a Population for Group II Disks with Gaps." *Astronomy and Astrophysics* 581 (September): A107. https://doi.org/10.1051/0004-6361/201525654.

Najita, J., J. S. Carr, R. D. Mathieu. 2003. "Gas in the Terrestrial Planet Region of Disks: CO Fundamental Emission from T Tauri Stars." *The Astrophysical Journal* 589, no. 2 (June): 931-952. https://doi.org/10.1086/374809.

Nelder, J. A. and Mead, R. 1965. "A Simplex Method for Function Minimization." *The Computer Journal* 8, Iss. 1 (April): 27. https://doi.org/10.1093/comjnl/8.1.27.

Pontoppidan, K. M. et al. 2008. "Spectroastrometric Imaging of Molecular Gas within Protoplanetary Disk Gaps." *The Astrophysical Journal* 684, no. 2 (September): 1323-1329. https://doi.org/10.1086/590400.

Pontoppidan, K. M., G. A. Blake, S. Alain. 2011. "The Structure and Dynamics of Molecular Gas in Planet-forming Zones: A CRIRES Spectroastrometric Survey." *The Astrophysical Journal* 733, no. 2 (June): 84. https://doi.org/10.1088/0004-637X/733/2/84.

Pascucci, I. et al. 2016. "A Steeper than Linear Disk Mass-Stellar Mass Scaling Relation." *The Astrophysical Journal* 831, no. 2 (November): 125-144. https://doi.org/10.3847/0004-637X/831/2/125.

Pinilla P. et al. 2018. "Homogeneous Analysis of the Dust Morphology of Transition Disks Observed with ALMA: Investigating Dust Trapping and the Origin of Cavities." *The Astrophysical Journal* 859, no. 1 (May): 32. https://doi.org/10.3847/1538-4357/aabf94.

Pontoppidan, K. M., C. Salyk, E. A. Bergin, S. Brittain, B. Marty, O. Mousis, K. I. Öberg. 2014. "Volatiles in Protoplanetary Disks." In *Protostars and Planets VI*, edited by Henrik Beuther, Ralf S. Klessen, Cornelis P. Dullemond, Thomas Henning, 363-385. Tuscon, Arizona: University of Arizona Press. https://doi.org/10.2458/azu_uapress_9780816531240-ch016.

Qi, Chunhua, K. I. Öberg, D. J. Wilner, K. A. Rosenfeld. 2013. "First Detection of c-C_3H_2 in a Circumstellar Disk." *The Astrophysical Journal* 765, no. 1 (March): L14. https://doi.org/10.1088/2041-8205/765/1/L14.

Rayner, J. et al. 2016. "iSHELL: A Construction, Assembly, and Testing." *Proceedings of the SPIE* 9908, (August): 17. https://doi.org/10.1117/12.2232064.

Rybicki, George B. and Alan P. Lightman. 2004. *Radiative Processes in Astrophysics*. Weinheim, Germany: WILEY-VCH Verlag GmbH & Co. KGaA.

Salyk, C., G. A. Blake, A. C. A. Boogert, and J. M. Brown. 2007. "Molecular Gas in the Inner 1 AU of the TW Hya and GM Aur Transitional Disks." *The Astrophysical Journal* 655, no. 2 (Februrary): L105-L108. https://doi.org/10.1086/512012.

Salyk, C., G. A. Blake, A. C. A. Boogert, and J. M. Brown. 2009. "High-Resolution 5 μm Spectroscopy of Transitional Disks." *The Astrophysical Journal* 699, no.1 (July): 330-347. https://doi.org/10.1088/0004-637X/699/1/330.

Salyk, C., G. A. Blake, A. C. A. Boogert, and J. M. Brown. 2011. "CO Rovibrational Emission as a Probe of Inner Disk Structure." *The Astrophysical Journal* 743, no. 2 (December): 112. https://doi.org/10.1088/0004-637X/743/2/112.

Sánchez, M. A., A. Banzatti, K. Hoadley, K. France, S. Bruderer. "Gas Evolution in Inner Disk Cavities from a Synergic Analysis of IR-CO and UV-H_2 Spectra." *Research Notes of the American Astronomical Society* 5, no. 4 (April): 78. https://doi.org/10.3847/2515-5172/abf43c.

Šimečková, Marie, D. Jacquemart, R. S. Laurence, R. R. Gamache, A. Goldman. 2005. "Einstein *A*-coefficients and Statistical Weights for Molecular Absorption Transitions in the HITRAN Database." *Journal of Quantitative Spectroscopy & Radiative Transfer* 98, (July): 130-155.

Taylor, John R. 1997. *An introduction to error analysis*. 2nd ed. California: University Science Books.

Testi, L. et al. 2014. "Dust Evolution in Protoplanetary Disks." In *Protostars and Planets VI*, edited by Henrik Beuther, Ralf S. Klessen, Cornelis P. Dullemond, Thomas Henning, 339-361. Tuscon, Arizona: University of Arizona Press. https://doi.org/10.2458/azu_uapress_9780816531240-ch015.

Thi, W. F., G. J. van Zadelhoff, E. F. van Dishoeck. 2004. "Organic Molecules in Protoplanetary Disks around T Tauri and Herbig Ae Stars." *Astronomy and Astrophysics* 425, (October): 955-972. https://doi.org/10.1051/0004-6361:200400026.

Turck and Chieze, S. et al. 2011. "The Long Term Dynamics of the Solar Radiative Zone associated to New Results from SoHO and Young Solar Analogs." *Astronomical Society of the Pacific* (September). https://ui.adsabs.harvard.edu/link_gateway/2011arXiv1109.4125T/arxiv:1109.4125.

Turner, N., S. Fromang, C. Gammie, H. Klahr, G. Lesur, M. Wardle, X. Bai. 2014. "Transport and Accretion in Planet-Forming Disks." In *Protostars and Planets VI*, edited by Henrik Beuther, Ralf S. Klessen, Cornelis P. Dullemond, Thomas Henning, 411-432. Tuscon, Arizona: University of Arizona Press. https://doi.org/10.2458/azu_uapress_9780816531240-ch018

van der Marel, Nienke, Jonathan P. Williams, and Simon Bruderer. 2018. "Rings and Gaps in Protoplanetary Disks: Planets or Snowlines?" *The Astrophysical Journal Letters* 867, no. 1 (October): L14-L21. https://doi.org/10.3847/2041-8213/aae88e.

van der Marel, Nienke, R. Dong, J. di Francesco, J. P. Williams, J. Tobin. 2019. "Protoplanetary Disk Rings and Gaps across Ages and Luminosities." *The Astrophysical Journal* 872, no. 1 (February): 112. https://doi.org/10.3847/1538-4357/aafd31.

van der Plas, G., F. Ménard, J. F. Gonzalez, S. Perez, L. Rodet, C. Pinte, L. Cieza, S. Casassus, M. Benisty. 2009. ALMA Study of the HD 100453 AB System and Tidal Interaction of the Companion with the Disk." *Astronomy and Astrophysics* 624, A33 (April). https://doi.org/.1051/0004-6361/201834134.

Vioque, M., R. D. Oudmaijer, D. Baines, I. Mendigutía, R. Pérez-Martínez. 2018. "Gaia DR2 Study of HerbigAe/Be Stars." *Astronomy and Astrophysics* 620 (December): A128. https://doi.org/10.1051/0004-6361/201832870.

Waters, L. B. F. M. 2015. "Dust in Protoplanetary Disks: Observations." *European Physical Journal Web of Conferences* 102 (September): 3. http://dx.doi.org/10.1051/epjconf/201510200003.